Thesis for the Degree of
Doctor of Philosophy in Engineering

Detection of Offshore Resources using Marine Controlled-source Electromagnetic Methods

by
Hangilro Jang

Department of Energy Resources Engineering
The Graduate School
Pukyong National University

February 26, 2016

Detection of Offshore Resources using Marine Controlled-source Electromagnetic Methods

(인공송신원 전자탐사법을 이용한 해저자원의 탐지)

Advisor: Prof. Hee Joon Kim

by
Hangilro Jang

A thesis submitted in partial fulfillment of the requirements
for the degree of

Doctor of Philosophy in Engineering

in Department of Energy Resources Engineering, The Graduate School,
Pukyong National University

February 26, 2016

Detection of Offshore Resources using Marine Controlled-source Electromagnetic Methods

A dissertation
by
Hangilro Jang

Approved by:

(Chairman) Wansoo Ha

(Member) Tae Jong Lee

(Member) Myung Jin Nam

(Member) Jeong-Sul Son

(Member) Hee Joon Kim

February 26, 2016

Detection of Offshore Resources using Marine Controlled-source Electromagnetic Methods

Hangilro Jang

Department of Energy Resources Engineering, The Graduate School,
Pukyong National University

Abstract

A marine controlled-source electromagnetic (CSEM) survey using an electric dipole in frequency domain has become popular for hydrocarbon (HC) exploration, where EM responses are directly related to the electrically resistive property of HC bearing strata in otherwise conductive marine sediments. Possible targets of the marine CSEM survey, other than HC or gas hydrate (GH) embedded in sediments, may be shallow sea-bottom sedimentation and hydrothermal mineral deposits under the deep sea.

Computer programs have been developed to evaluate EM responses for a one-dimensional (1D) model with multiple source and receiver dipoles that are finite in length in both frequency- and time-domain. The time-domain solution can be obtained by applying an inverse fast Fourier transform (FFT) to frequency-domain fields for efficiency. Frequency-domain responses are first obtained for 10 logarithmically equidistant frequencies per decade, and then cubic spline interpolated to get the FFT input. The phase curve must be made to be continuous prior to the spline interpolation. The spline interpolated data are convolved with a source current waveform prior to FFT.

Using the frequency-domain code, I conducted sensitivity analysis of marine CSEM methods to a GH layer in the shallow section. From these numerical experiments, I found that there are plenty of useful offset ranges and frequencies where amplitude difference is large enough to detect the target

layer. Furthermore, an effect of airwaves is almost absent in amplitude difference.

With the use of time-domain code, I calculated step-off responses for 1D HC reservoir models. Although the vertical electric field has much smaller amplitude of signal than the horizontal field, vertical currents resulting from a vertical transmitter are sensitive to resistive layers. The modeling showed a significant difference in step-off responses between HC- and water-filled reservoirs, and the contrast can be recognized at late times at relatively short offsets. A maximum contrast occurs at more than 4 s, being delayed with the depth of the HC layer.

I examined step-off responses for a layered model and compare the characteristics of horizontal and vertical loop systems for detecting hydrothermal deposits. The feasibility study showed that transient EM (TEM) responses are very sensitive to a highly conductive layer. Time-domain target responses are larger and appear earlier in horizontal magnetic fields than in vertical ones, although the vertical field has 2 – 3 times larger magnitude than the horizontal one. An inverse problem is formulated with the Gauss-Newton method and solved with the damped and smoothness-constrained least-squares approach. The test example for a marine hydrothermal TEM survey demonstrated that the depth extent, conductivity and thickness of the highly conductive layer are well resolved.

Finally, I investigated the 3D frequency-domain electromagnetic responses of a 100 m thick, 5 km in diameter disk-shaped hydrocarbon reservoir buried at a depth of 1 km below the seafloor. From the numerical results, I recognized that a 3D effect of the reservoir typically produces a transition zone in comparison with 1D model responses. The transition zone decreases with the airwave effect as the depth of water becomes shallow. As the source frequency increases, the sensitivity to the reservoir increases, whereas the amplitude decreases and falls at higher than 1 Hz below the current system noise floor. Broadside electric fields for a 10-km diameter disk model are only about 5 % of

in-line electric fields for the 5-km disk model. The T-equivalence is observed at such a low frequency of 1 Hz for the thin resistive tabular target, whose response varies almost linearly with the target thickness and resistivity even in the transition zone.

Keywords: marine CSEM, gas hydrates, hydrocarbon reservoirs, airwave, hydrothermal deposits, transient EM

Contents

List of figures

depth of 1000 m. The resistive HC layer is buried at 1000 m below the seafloor.

Fig. 4.4. Step-off responses for various offsets between the source and receiver over the HC reservoir model (solid lines) and the background model (dashed lines). The bottom lines indicate the ratios between the responses of the HC reservoir and the background models. A 100 m-long transmitter and 10 m-long receiver are located on the seafloor with a water depth of 1000 m. The resistive HC layer is buried at 1000 m below the seafloor.

Fig. 4.5. Step-off responses for various water depths over the HC reservoir model (solid lines) and the background model (dashed lines). The bottom lines indicate the ratios between the responses of the HC reservoir and the background models. A 100 m-long transmitter and 10 m-long receiver are located on the seafloor and the offset is 500 m. The resistive HC layer is buried at 1000 m below the seafloor.

Fig. 4.6. Step-off responses for various depths of the resistive HC layer over the HC reservoir model (solid lines) and the background model (dashed line). The bottom lines indicate the ratios between the responses of the HC reservoir and the background models. A 10 m-long receiver is located 500 m away from a 100 m-long transmitter on the seafloor with a water depth of 1000 m.

Fig. 4.7. Step-off responses for various source lengths over the HC reservoir model (solid lines) and the background model (dashed lines). The bottom lines indicate the ratios between the responses of the HC reservoir and the background models. A 10 m-long receiver is located 500 m away from the transmitter on the seafloor with a water depth of 1000 m. The resistive HC layer is buried at 1000 m below the seafloor.

Chapter 1. Introduction

1.1. Background and motivation

The great progress in computation and instrumentation has been made it possible to apply a controlled-source electromagnetic (CSEM) method for offshore exploration. In the early days, the marine CSEM method carried out to determine conductivity of oceanic lithosphere (Cox et al., 1986). Since, it began to be known that the marine CSEM method is very useful to detect a resistive medium such as hydrocarbon (HC) and gas-hydrate (GH), the major oil companies have been showed great interests in the method. First successful commercial exploration in the Angola region accelerated the development of the technology and recently has become an important exploration tool for the HC industry (Ellingsrud et al., 2002, Constable, 2010). Furthermore, Bhuyian et al. (2012) and Kang et al. (2012) showed the feasibility of the offshore CO_2 sequestration monitoring.

A significant problem in CSEM is posed by the so called airwave. It consists of an EM field, which diffuses vertically upward in the water layer and is refracted at the air-water interface (Hunziker et al., 2011). Due to the extremely low conductivity in air, the field propagates in the air as a wave with the speed of light. Because the EM skin depth is almost always smaller in seawater than in subseafloor sediments, the EM fields measured by receivers have propagated almost entirely beneath the seafloor at a sufficiently long source-receiver offset. However, this desirable sensitivity to subseafloor geology can be significantly lower in shallow water and at higher frequencies, where the air layer brings a stronger influence on the data. This airwave effect (energy propagating from source to receiver via the atmosphere) may be comparable or larger than the signal through the subseafloor (Um and Alumbaugh, 2007). Thus, the accurate evaluation of the airwave is essential to

extract the desired information about subseafloor geology from marine CSEM measurements.

The most fundamental aspect of the offshore exploration problem is that hydrocarbons are electrically resistive while porous seafloor sediments saturated with saline water are conductive. A typical reservoir is therefore a thin resistive target in a conductive background. Whereas the magnetotelluric method has predominantly horizontal electric current flow and is well known to be insensitive to thin resistors, the vertical current loops created by CSEM transmitters can be interrupted by thin resistive layers, creating a detectable increase in the EM field observed on the seafloor. Since there is much less inductive attenuation in a resistive reservoir compared to the surrounding conductive sediments, the EM fields will preferentially diffuse through the reservoir (Key, 2012). Electrical resistivity of marine sediments is mainly controlled by the amount of seawater in the available pore space, the porosity. Gas hydrates are electrically more resistive than the marine sediments. Therefore, they will have an EM signature that increases with hydrate volume fraction. Indeed, well logs indicate increased resistivity in zones of gas hydrate, although this effect is sometimes modest (Gabitto and Tsouris, 2010). Marine EM methods are able to augment seismic data to provide valuable information about gas hydrate distribution in the marine environment (Weitemeyer et al., 2006).

There is another growing interest in detection of seafloor massive sulfide deposits under the deep sea, other than HC or GH, using the marine CSEM survey. It is well known that the transient electromagnetic (TEM) method is sensitive to conductive targets at depth and uses the concept of the “smoke ring” (Nabighian and Macnae, 1991). Nowadays, marine CSEM methods are using to detect various offshore resources (Key, 2012), while early academic applications focused on measuring the conductivity of the lithosphere (Cox et al., 1986).

1.2. Thesis overview

In Chapter 2, a new 1D EM modeling code with multiple source and receiver dipoles that are finite in length is presented. The transient responses are obtained by applying a Fourier transform to frequency-domain fields.

With the use of the frequency-domain modeling code presented in Chapter 2, I examine the sensitivity of the CSEM method to a weakly resistive layer buried in shallow conductive sediments in Chapter 3.

In Chapter 3, I examine the sensitivity of the CSEM method to a weakly resistive layer buried in shallow conductive sediments by using the frequency-domain modeling code presented in Chapter 2.

The time-domain modeling code is also used to investigate vertical transient EM responses from a vertical transmitter for offshore HC reservoir models in Chapter 4.

In Chapter 5, I investigate the possibility of applying an in-loop TEM system to the detection of marine hydrothermal deposits with a thin sediment cover. We analyze step-off responses of variable parameters for a layered model and compare the characteristics of horizontal and vertical loop systems for detecting a highly conductive layer. Then, two inversion techniques are tested to recover the highly conductive layer from TEM sounding data.

In Chapter 6, I present a 3D marine CSEM modeling algorithm assuming primary EM fields as those in a homogeneous half-space to account for airwave effects exactly, and then examine the sensitivity of marine CSEM methods to a thin resistive disk-shaped target buried in the conductive media.

The concluding Chapter summarizes the conclusions in the previous Chapters.

Chapter 2. Modeling of electromagnetic responses

2.1. Introduction

A layered-earth solution of frequency-domain electromagnetic (EM) responses can be calculated using a computer code EM1D (Kim et al., 1997, Song et al., 2002), one of the most popular software applications in the EM community. However, since these responses are to a point dipole source, Lee et al. (2011) modified the code to suit a marine controlled-source electromagnetic (CSEM) model with a realistic source dipole that is finite in length.

In this Chapter, I present a new one-dimensional (1D) time-domain modeling code with multiple source and receiver dipoles that are finite in length. The transient EM responses are obtained by applying a Fourier transform to frequency-domain fields.

2.2. Frequency-domain responses

Maxwell's equations with $e^{i\omega t}$ time dependence are given by

$$\nabla \times \mathbf{E} = -i\omega\mu_0 \mathbf{H} - i\omega \mathbf{M}_s \tag{2.1}$$

$$\nabla \times \mathbf{H} = (\sigma + i\omega\varepsilon)\mathbf{E} + \mathbf{J}_s \tag{2.2}$$

where **E** and **H** are the electric and magnetic fields, respectively, $\mathbf{J}_s$ and $\mathbf{M}_s$ represent the electric and magnetic sources, respectively, ω is the angular frequency, μ_0 (= $4\pi\times10^{-7}$) is the magnetic permeability of the free space, σ is the conductivity, and ε is the permittivity. From equations (2.1) and (2.2), a second-order vector Helmholtz equation for the electric field in low-frequency limit can be obtained as

$$\nabla \times \nabla \times \mathbf{E} + i\omega\mu_0\sigma\mathbf{E} = -i\omega\mu_0 \mathbf{J}_s - i\omega\nabla \times \mathbf{M}_s \tag{2.3}$$

The analytic solution for the EM fields of a point source such as an electric dipole in the presence of layered earth can be simplified if the solution is developed in terms of transverse electric and transverse magnetic modes.

Because changes in physical properties coincide with coordinate surfaces (planes of constant z) we can solve the boundary-value problem by converting the partial differential equation to an ordinary differential equation in z. This conversion takes the form of a Hankel or 2D Fourier transform since the coordinate surfaces are infinite in extent in the x and y directions. The solution in Fourier transform space can be derived using the plane-wave impedance formulas for a layered earth. Then, the final solution obtained by inverse Fourier or Hankel transformation (Ward and Hohmann, 1987).

In general, the source and the receiver are considered as a set of finite-length dipoles. The resulting electric field may be obtained by numerically integrating along all the source and receiver dipoles. Symbolically, it can be written as

$$E_{\mathrm{EM1D}-f} = \sum_{jr=1}^{NR}\sum_{j=1}^{NJ} w_{j,jr} l_{j,jr} \sum_{ir=1}^{NS}\sum_{i=1}^{NI} w_{i,ir} l_{i,ir} E_{\mathrm{EM1D}}(r_{j,jr}, r_{i,ir}) \tag{2.4}$$

Here, NS is finite-length sources and NR is finite-length receivers. Each source and receiver is then divided into NI and NJ segments, respectively, short enough to be considered point dipoles. Coefficients $w_{i,ir}$ and $w_{j,jr}$ are the weights typically used for the numerical integration, and $l_{i,ir}$ and $l_{j,jr}$ are the lengths of the source and receiver segments. A trapezoidal rule is used for the weighting. The actual summation process involves one more step in addition to the above expression because an arbitrarily oriented dipole consists of three Cartesian components, both for the source and the receiver.

To define a finite-length dipole in model domain, Cartesian coordinates of two end points of the dipole are used as input. The direction of current flow or

the voltage measurements are dictated by the order of input of the end points. The accuracy of the numerical summation largely depends on how finely the given dipoles are divided. It depends on the source-receiver dipole separation and the frequency used, but only the dipole separation is considered under current development.

2.3. Time-domain responses

Transient EM responses, e(t), can be obtained from an inverse Fourier transform of frequency-domain responses, E(ω),

$$e(t) = \frac{1}{2\pi}\int_{-\infty}^{\infty} E(\omega)e^{iwt}d\omega, \tag{2.5}$$

where ω is the angular frequency. The time-domain solution in equation (2.5) is evaluated by a fast Fourier transform (FFT) for efficiency. Frequency-domain responses are first obtained for a selected number of frequencies, e.g. 10 logarithmically equidistance samples per decade, and then spline interpolated to get the FFT input. In the code developed by Jang et al. (2013), one can choose from one of the four current waveforms: step-off, square, impulse, and INPUT (see Appendix A). Ramp time is optional to the step-off or square waveform, and its shape is linear in time. The frequency-domain result is obtained from the code developed by Lee et al. (2011) to include multiple source and receiver dipoles that are finite in length.

The lowest (fundamental) frequency used in FFT is determined by the period (T) of a chosen waveform as 1/T. The highest (Nyquist) frequency is not directly related to the waveform. To achieve minimally aliased and accurate time-domain results, one needs to get high enough frequency data and use them in the inverse Fourier transform. Selection of the highest frequency limit can be safely done by making sure that the minimum source-receiver distance is more

than 10 skin depths over which EM fields are expected to be sufficiently attenuated.

The method of calculating time-domain responses from frequency-domain responses by an inverse Fourier transform is a well-known technique in seismic and EM surveys. In particular, since EM responses are complex in frequency domain, they are represented as

$$E(\omega) = R(\omega) + I(\omega), \tag{2.6}$$

where R and I indicates the real (in-phase) and imaginary (out-of-phase or quadrature) components, respectively, and ω (= $2\pi f$) is the angular frequency. Furthermore, they can be divided into

$$A(\omega) = \sqrt{R(\omega)^2 + I(\omega)^2}, \tag{2.7}$$

and

$$P(\omega) = \tan^{-1}\frac{I(\omega)}{R(\omega)}, \tag{2.8}$$

where A and P indicates the amplitude and phase, respectively. In general, log$A$ and P (radian) are sampled at logarithmically equidistant frequencies (log$f$). In this study, 10 samples are obtained per decade. The reason why the logarithmic transformation is applied only to the amplitude is that it varies significantly with frequency, and thereby the variation range of log$A$ and P becomes similar.

When we use FFT for computational efficiency, frequency-domain responses should not be sampled logarithmically but linearly. It is efficient to use an interpolation method for linear sampling from logarithmically equidistant data. In this study, a cubic spline interpolation method with a third-order polynomial is used to fill log$A$ and P at desired frequencies (e.g., Press et al., 1992). However, since the arctangent in equation (2.8) is limited to a range

of $-\pi$ to π, the phase varies abruptly at the limit at $-\pi$ or π, where a sign reversal occurs in *R* or *I*. In order to confirm the abrupt change in phase, which may cause troubles in the course of interpolation, I examine a model shown in Fig. 2.1. The model consists of 0.3 ohm-m seawater with a depth of 1000 m and 1 ohm-m seafloor sediments. A 10 m-long, vertical receiver and a 100-m vertical transmitter are located on the seafloor and the horizontal offset is 500 m. Vertical sources have an advantage of not producing airwaves and are sensitive to a horizontal resistive target within the earth (Edwards et al., 2007; Holten et al., 2009; Hunziker et al., 2011).

Fig. 2.2 represents phases prior to interpolation at logarithmically equidistant frequencies for the model shown in Fig. 2.1, which is needed to calculate a vertical electric field, e_z, in time domain. The phase (symbol ◊) obtained from equation (2.8) shows a sudden jump from $-\pi$ to $+\pi$ at about 5 Hz. This is due to the simple application of equation (2.8) to the phase estimation. If an interpolation technique is applied to this discontinuity in phase without any processing, it is likely to get an incorrect value. In practice, Fig. 2.3 shows e_z in time domain obtained from E_z in frequency domain which are derived from spline interpolated log*A* and *P*. From the illustration, one can see that the time-domain response oscillates after 0.1 s. It is clear that this is due to the interpolation of discontinuous phases.

In order to avoid the phase problem, we should make the phase curve continuous as shown by symbol o in Fig. 2.2. To this end, subroutine DRUM is useful (Robinson, 1967; Appendix B). Fig. 2.3 also shows time-domain vertical electric fields obtained after correcting the discontinuity in phase with subroutine DRUM. From the illustration, one can see that the electric field decreases monotonically even after 0.1 s.

As described above, since amplitude *A* is generally transformed into log*A*, the interpolation process is also applied to log*A* and then the time-domain EM response is obtained after restoring *A*. However, such a procedure may cause a

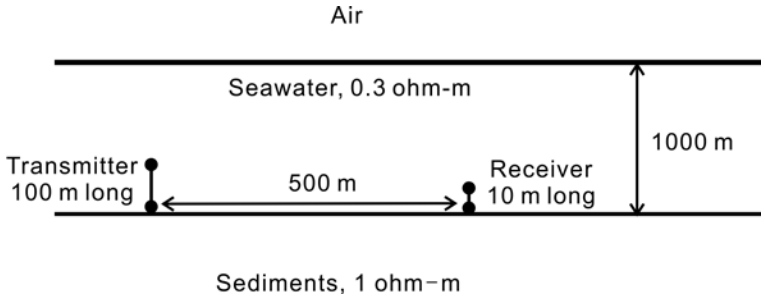

Fig. 2.1. A two-layered offshore model consisting of 0.3 ohm-m seawater with a depth of 1000 m and 1 ohm-m seafloor sediments. A 10 m-long, vertical receiver and a 100-m vertical transmitter are located on the seafloor and the horizontal offset is 500 m.

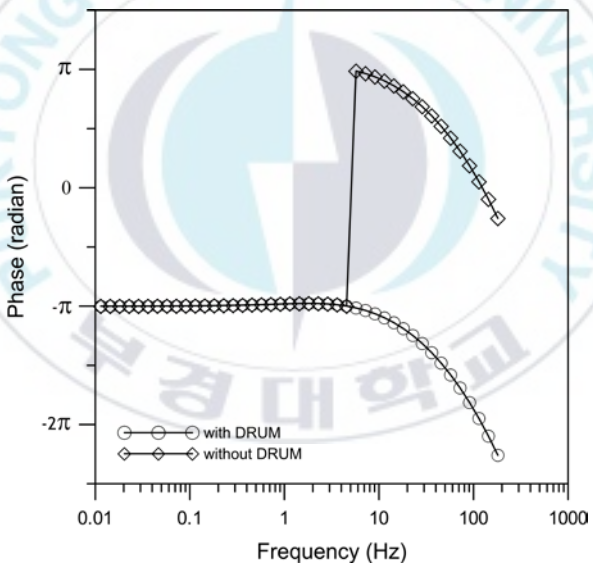

Fig. 2.2. Phase responses for the two-layered model shown in Fig. 2.1. Circle and diamond symbols indicate the responses calculated using the codes with and without subroutine DRUM, respectively.

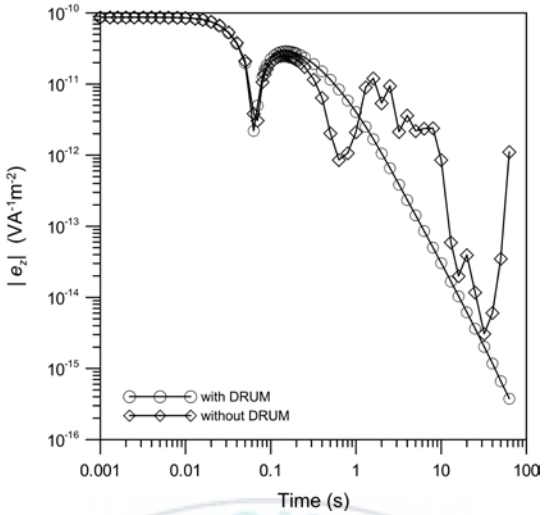

Fig. 2.3. Vertical electric fields for the two-layered model shown in Fig. 2.1. Symbols are the same as in Fig. 2.2.

numerical error at late times. As an example, Fig. 2.4 shows horizontal magnetic fields in time domain for the model shown in Fig. 2.1. It is well known that at late times t the horizontal magnetic field and vertical electric field decays as $t^{-5/2}$ in a homogeneous half-space (Ward and Hohmann, 1987; Jang et al., 2013), but the result using log$A$ (symbol o) deviates gradually from a $t^{-5/2}$ asymptote after about 100 s as in Fig. 2.5. A solution to overcome this problem is simple than expected. When using A itself in the interpolation process instead of log$A$, the error is largely decreased as in Fig. 2.5 (symbol +).

Another method for calculating the time-domain response is applying the cubic spline interpolation method directly to the real and imaginary parts of the frequency-domain response. It was expected that this simple technique would produce incorrect values, because the real and imaginary parts have sign reversals with frequency. However, the result is accurate enough similar to that of using the amplitude and phase at least in the case of marine CSEM.

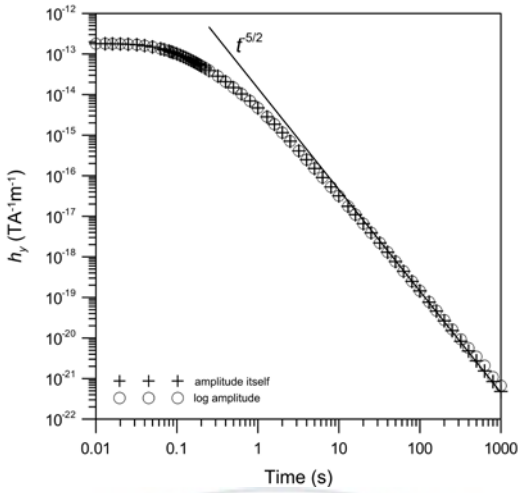

Fig. 2.4. Horizontal magnetic fields for the two-layered model shown in Fig. 2.1. Circle and cross symbols indicate the responses derived using log amplitudes and amplitude themselves, respectively and solid line represents asymptotic values proportional to $t^{-5/2}$.

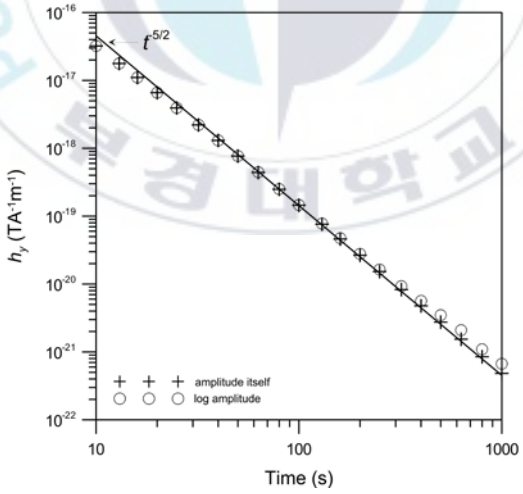

Fig. 2.5. Same as in Fig. 2.4 but showing the time range from 10 s to 1000 s.

A horizontal step-off response of the inline electric field, $e_x(t)$, from a unit horizontal source dipole at the surface of a homogeneous half-space is given by (Spies and Frischknecht, 1991)

$$e_x(t) = \frac{1}{2\pi\sigma r^3}\left[\operatorname{erf}(\theta r) - \frac{2}{\sqrt{\pi}}\theta r \exp(-\theta^2 r^2)\right], \tag{2.9}$$

where

$$\theta = \sqrt{\frac{\sigma\mu_0}{4t}}, \quad \mu_0 = 4\pi \times 10^{-7} \text{ H/m},$$

σ is the conductivity of the homogeneous half-space, r is the distance between source and receiver and erf(·) denotes the error function.

Using an asymptotic expression of the error function for the early time $t \rightarrow 0$, one can get the early-time step-off response

$$e_x(0) = \frac{1}{\pi\sigma r^3}. \tag{2.10}$$

Then the normalized (dimensionless) step-off response is given by

$$\frac{e_x(t)}{e_x(0)} = \frac{1}{2}\operatorname{erf}(\theta r) - \frac{\theta r}{\sqrt{\pi}}\exp(-\theta^2 r^2). \tag{2.11}$$

Fig. 2.6 shows normalized step-off transient responses for a homogeneous half-space with resistivities of 0.1, 0.3, 1, 3 and 10 ohm-m. Both the transmitter and receiver are situated at the surface of the half-space and the offset is 1000 m. In the case of 0.3 ohm-m, for example, 41 logarithmically equidistant samples are first obtained, and then spline interpolated to get 8192 data for FFT input. The solid lines indicate the analytic solution given in equation (2.11),

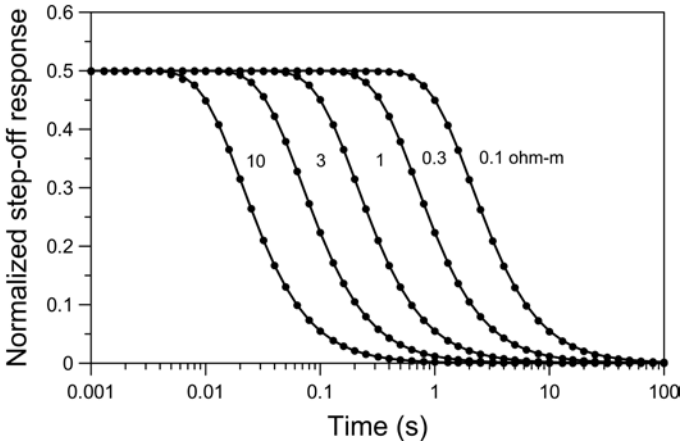

Fig. 2.6. Normalized step-off responses at the surface of the homogeneous half-space. Solid lines indicate the analytic solution and dots are numerical results from a digital filter.

and the dots represent the results from the 1D code described above. The agreement is fairly good.

2.4. Conclusions

In this Chapter, I have developed a frequency- and time-domain forward modeling code. Simple 1D modeling is an efficient way to obtain an indication of the likely source–receiver offsets necessary to detect a resistive target (Constable and Weiss, 2006; Connell and Key, 2012). The time-domain EM responses can be efficiently computed by a spline interpolation and a fast Fourier transform of the frequency-domain EM responses with multiple source and receiver dipoles that are finite in length (Lee et al., 2011). The key component of my modeling study is a solver that gives the time-domain CSEM response over a 1D layered model. This solver is fast and thus easily employed in any standard inversion scheme.

Chapter 3. Sensitivity analysis of marine controlled-source electromagnetic methods to a shallow gas-hydrate layer

3.1. Introduction

Natural gas hydrates, originally discovered in Arctic permafrost, are ice-like solids that exist worldwide in seafloor sediments along continental margins. They consist of gas molecules, mainly methane, contained in a cage-like structure of water molecules. They form under conditions of low temperature and high pressure, typically in the uppermost few hundreds of meters of sediments in water depths exceeding 500 m. The global abundance of methane frozen in hydrate exceeds the amount of all other known fossil hydrocarbon resources (Kvenvolden, 1993; 1999). Although gas hydrates are recognized as an important possible future energy resource, methane is a powerful greenhouse gas and may contribute to global warming if released into the atmosphere. In addition, marine gas hydrates can contribute to slope instability, which may threaten seafloor infrastructure.

A gas hydrate deposit can be generally identified in a seismic section as a bottom simulating reflector (BSR) which is associated with the base of a hydrate stability zone (HSZ). This lower stratigraphic boundary is a transition zone between hydrate bearing sediments above it and free gas and water below it. The location of HSZ is temperature controlled and depends on the ambient geothermal gradient. The diffuse upper boundary is not as well marked so that the total mass of hydrate is not determined easily by seismic alone, and there is generally no seismic signature from the hydrate volume.

Electrical resistivity of marine sediments is mainly controlled by the amount of seawater in the available pore space, the porosity. It is typically around 1 ohm-m right beneath the seafloor. Because hydrate itself is an electrical insulator and forms in the available pore space within HSZ replacing conductive pore fluid, electrical resistivity can rise significantly (Edwards, 1997; Weitemeyer et al., 2006). Electrical resistivity measurements made in well logs characterize a region containing hydrate as more resistive when compared to background sediments without hydrate. Needless to say, drilling is expensive and drilling into hydrates can be hazardous, destabilizing HSZ.

For gas hydrate characterization a short-offset time-domain electric dipole-dipole system was used in the Cascadia margin off the coast of Vancouver Island, British Columbia, Canada (Yuan and Edwards, 2000; Schwalenberg et al., 2005). In contrast, Weitemeyer et al. (2006) employed a frequency-domain CSEM method to detect gas hydrates at Hydrate Ridge, offshore Oregon. In this Chapter, I examine the sensitivity of the controlled-source electromagnetic (CSEM) method to a weakly resistive layer buried in shallow conductive sediments using a one-dimensional (1D) forward modeling code with multiple source and receiver dipoles that are finite in length.

3.2. Method

The basis of marine CSEM is the use of a mobile horizontal electric dipole (HED) source and an array of electric- and magnetic-field receivers on the seafloor (Fig. 3.1; Weitemeyer et al., 2006). The transmitter generates a low-frequency (typically a few to a few hundreds of Hz) EM field, which propagates both upwards in the seawater and downward within the sub-seafloor. The rate of decay in amplitude and the phase shift of the signal are controlled by both geometric and skin depth effects (Constable and Srnka, 2007). Because in general the seabed is more resistive than seawater, skin depths in the seabed are longer. As a result, EM fields at a sufficient source-

receiver distance are dominated by energy propagating through the seabed. HED can excite both vertical and horizontal current flow in the seabed, maximizing resolution for a variety of structures (e.g., Constable and Srnka, 2007).

Transmitted EM signals are directly proportional to the source dipole moment, in turn given by the dipole length times the emission current. Data for interpretation are normalized by the dipole moment, so the system noise floor gets lower as the moment gets larger, allowing larger source-receiver offsets to be recorded and deeper structure to be detected. Dipole lengths are typically 100 – 300 m (Constable, 2006); making them significantly longer than that would make towing transmitter dipole close to the seafloor a technologically challenging proposition. Electric field measurements are made across electrodes mounted at the ends of plastic arms about 10 m across (Constable, 2006).

Using a 3D modeling algorithm, Weiss and Constable (2006) demonstrated that if both source and receivers are over a tabular 3D resistive target, 1D modeling predicts the observed response to very high accuracy. Experimental design can thus be based on 1D analysis to find the optimal survey parameters for a given target structure (Weitemeyer et al., 2006; Kang et al., 2010).

3.3. Gas hydrates responses

The detection capability of a gas hydrate layer depends on the frequency used and the source-receiver configuration. Fig. 3.2 shows a typical 1D marine CSEM model where the target layer is buried below the seafloor with varying depth of burial. This model is chosen on the basis of well logs gathered during ODP Leg 204 (Tréhu et al., 2006). I first considered a 1000-m seawater depth and BSR at a depth of 150 m below the seafloor. A 100 m-thick hydrate layer with a resistivity of 2 ohm-m is buried in a 1 ohm-m background sediment. A finite-length HED source is towed at variable height above the seafloor.

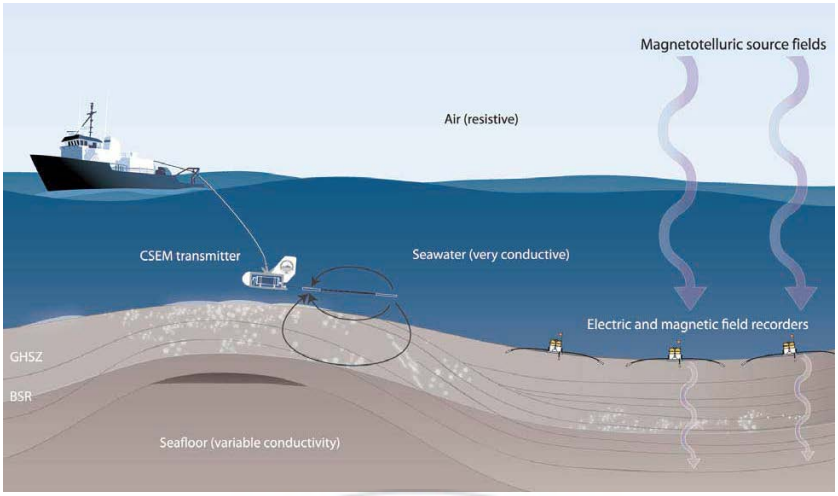

Fig. 3.1. An electric dipole transmitter is towed above the seafloor (~100 m) and an alternating EM field is transmitted along the antenna, which can be 100 – 300 m long. Seafloor receivers record electric fields (and magnetic fields) from the transmitter. BSR = bottom simulating reflector; GHSZ = gas hydrate stability zone (After Weitemeyer et al., 2006).

In this study, I use normalized amplitude and amplitude difference simultaneously in determining the detection capability of the hydrate layer. The normalized amplitude is the field amplitude of a hydrate model response normalized by that of the model without the hydrate layer, the background model (Eidesmo et al., 2002), while the amplitude difference is the difference in amplitude between responses of the hydrate and background models (Kong et al., 2008).

EM fields from a transmitter decay rapidly, a combination of $1/r^3$ dipole geometry (r: transmitter-receiver distance) and exponential inductive attenuation. Because CSEM field amplitudes ($VA^{-1}m^{-2}$) vary over such a large

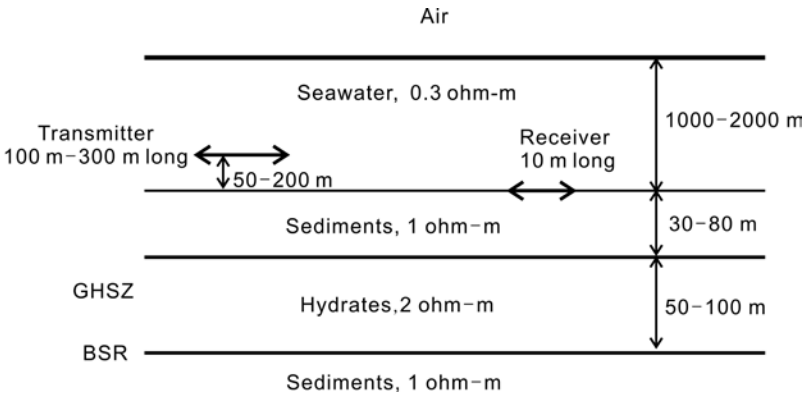

Fig. 3.2. 1D marine CSEM model with variable depth to a resistive hydrate layer, and source length and altitude above the seafloor. EM fields are calculated for the model as a function of the transmitter-receiver separation and frequency.

range, it is useful to consider fields normalized by a background response, which is produced in the absence of the hydrate layer. The reasoning behind the employment of normalized amplitude for the analysis is that the larger it gets the easier one can differentiate the model from the background model. At the same time though, one should remember that the voltage signal must be larger than a threshold before a marine CSEM system can read it. This limit is on the order of 10^{-15} $VA^{-1}m^{-2}$ (Constable and Srnka, 2007). The normalized amplitude can be numerically very large on the computer, but if the amplitudes of electric fields are smaller than the threshold, it cannot even be measured and therefore is useless.

The target structure is seen over a limited range of frequency and source-receiver offset in the radial mode obtained from the in-line geometry as shown in Fig. 3.3. Frequencies below 10 Hz do not produce large effects because there is little induction in the target layer, and large electric fields are dominated by the water and sediment. At frequencies above 1000 Hz, skin depth in the

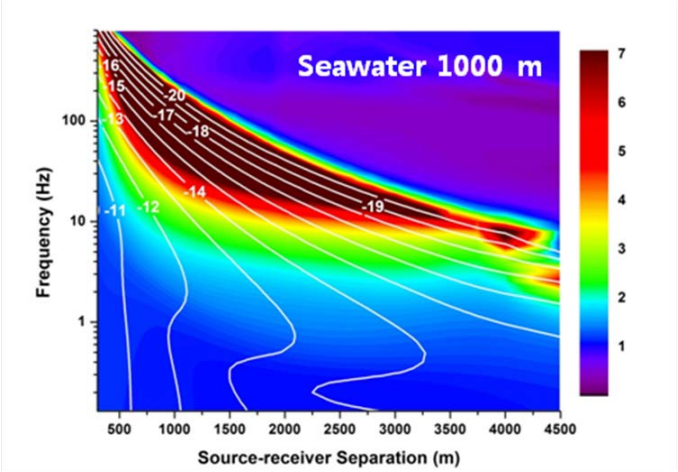

Fig. 3.3. Normalized amplitude (in color shade) and amplitude difference (in line contour, $VA^{-1}m^{-2}$) in radial mode for the hydrate model in Fig. 3.2. The hydrate layer is buried at a depth of 50 m. The source dipole length is 100 m and its altitude is 100 m above the seafloor.

sediment is only 16 m, and most energy is absorbed in the seawater and overburden. An effect of airwaves is only recognized in an offset range longer than 3500 m in normalized amplitude, in which electric fields are below the current instrument system noise floor. The airwave effect disappears if the water depth is increased to 2000 m as in Fig. 3.4. In contrast, the airwave effect is almost absent in amplitude difference (compare Figs. 3.3 and 3.4). This is one of the reasons of using amplitude difference as a hydrate detection capability.

As mentioned above, data which show large normalized amplitudes are useful for detecting gas hydrates, provided that the actual amplitude of the field data is well over the noise threshold. Equally important, as we will find out in a moment, is the amplitude difference. Normalized amplitudes are hardly greater than 2.0 at frequencies below 10 Hz but amplitude differences are larger

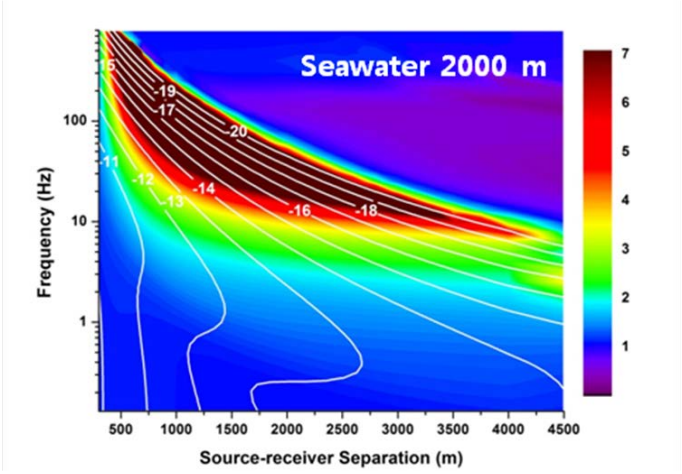

Fig. 3.4. Same as in Fig. 3.3 except that the water depth is 2000 m.

than 10^{-15} $VA^{-1}m^{-2}$, which is above the noise floor, at offsets shorter than 2000 m (Fig. 3.3). These differences are on the order of a few parts per thousand of actual field amplitudes, the reason why one cannot easily tell the difference between them graphically, but can be useful data for extracting information about the hydrate layer, although this would of course require accurate data acquisition. Because the useful anomalies can be obtained at shorter offsets, it may be dangerous if we ignore the effect of dipole length.

The normalized response in Fig. 3.3 is quite similar to that obtained from a point source response (e.g., Weitemeyer et al., 2006; Kang et al., 2010). This means that the effect of dipole length is neglected almost completely if we use the normalized amplitude in the model study. If the effect of dipole length is ignored from a background half-space model, to which real field data are normalized, however, the thickness of the hydrate layer may be overestimated because elevated electric-field responses especially at short offsets persist indefinitely off the upper boundary of the target layer. Fig. 3.5 shows the effect of dipole length on the normalized amplitude and the amplitude difference. The

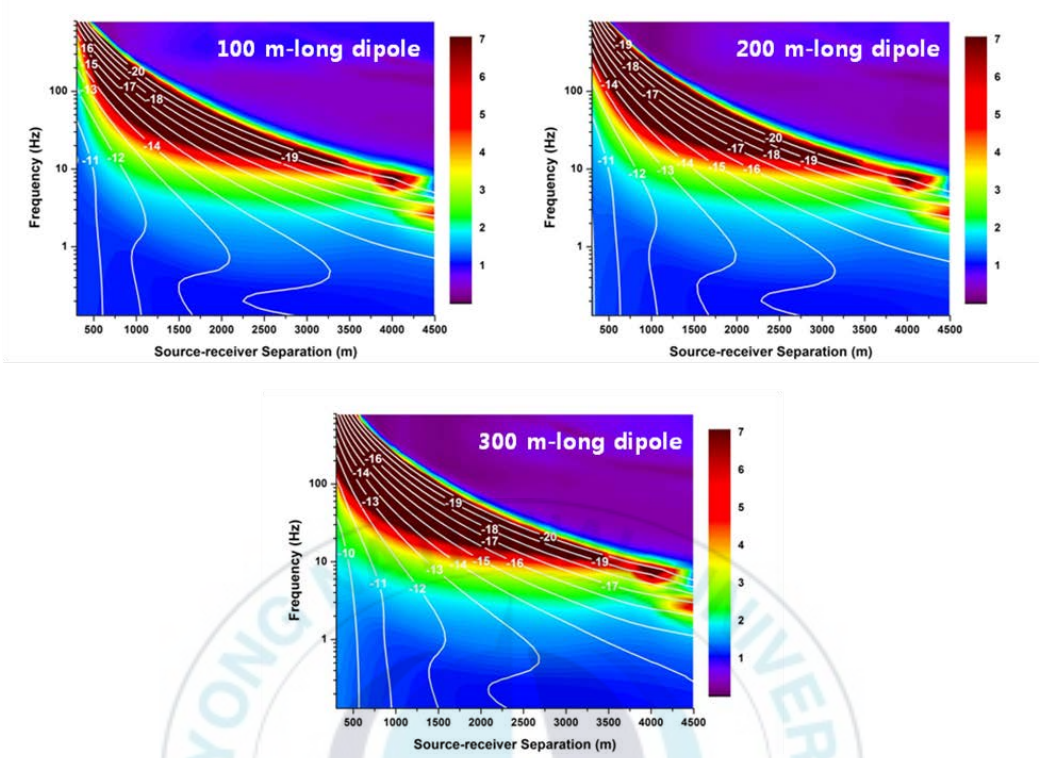

Fig. 3.5. Same as in Fig. 3.3 except that the background model is excited by a point dipole source. Three source dipole lengths are considered: (a) 100 m, (b) 200 m, and (c) 300 m.

target signal is distorted compared with Fig. 3.3 especially at higher frequencies and longer dipoles.

Comparing Fig. 3.6 to Fig. 3.3, we can find that a magnetic field anomaly in terms of the normalized amplitude is quite similar to the electric field anomaly for the same model. Because magnetic field measurements are made using an induction coil in the form of d*B*/d*t*, the voltage conversion is given by

$$V \text{ in Volt} = \omega \times \text{magnetic field in } \gamma\ (= \text{nT}) \times 10^{-9}$$

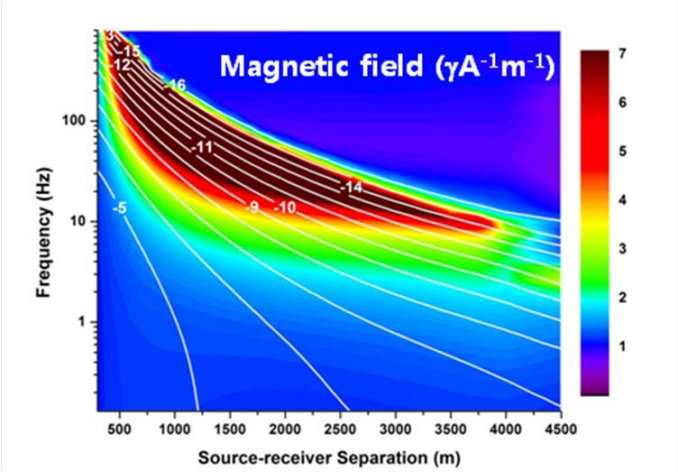

Fig. 3.6. Normalized amplitude (in color shade) and amplitude difference (in line contour) in magnetic fields ($\gamma A^{-1}m^{-1}$) for the hydrate model in Fig. 3.2. The hydrate layer is buried at a depth of 50 m. A 100 m-long dipole source is situated at 100 m above the seafloor.

So, a magnetic field of 10^{-7} at 10 Hz is equivalent to 2×10^{-15} V, assuming that the effective moment of receiver coil is unity. This is well above the electric field noise floor. Magnetic field measurements are made in marine CSEM methods, but motion of the sensors as water currents move the receiver instrument limits the noise floor (Constable and Srnka, 2007).

Much has been made of the different behavior of the radial and azimuthal modes in the case of a deep thin resistor (e.g., Constable and Weiss, 2006), whereby the radial mode has a larger oil reservoir response than the azimuthal mode. Constable and Srnka (2007) explained this different behavior at relatively low frequencies that CSEM fields are dominated by the galvanic response of the reservoir, i.e., charge accumulation on the surface of the resistive layer associated with vertical current flow from the transmitter in the radial mode, which is largely absent in the azimuthal mode. In contrast, inductive effects dominate in the azimuthal fields and the observed response

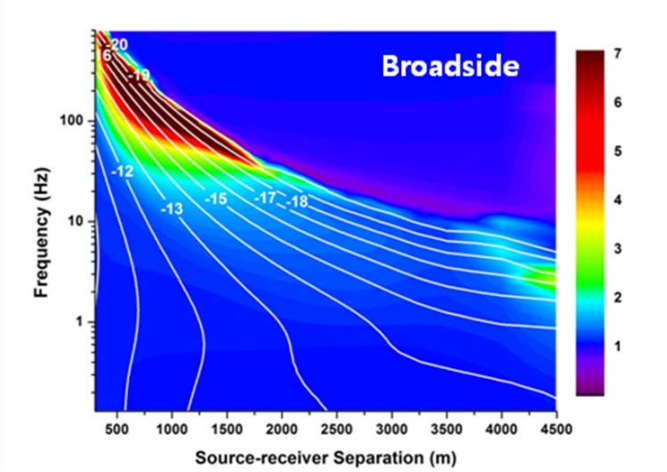

Fig. 3.7. Normalized amplitude (in color shade) and amplitude difference (in line contour, $VA^{-1}m^{-2}$) in azimuthal mode for the hydrate model in Fig. 3.2. The hydrate layer is buried at a depth of 50 m. A 100 m-long dipole source is situated at 100 m above the seafloor.

can in general be explained in terms of attenuative effects governed by EM skin depth.

When the frequency is high enough, inductive effects in the hydrate layer produce a significant response in the azimuthal mode obtained from the broadside geometry as shown in Fig. 3.7. The reduced signal below 100 Hz compared with the radial fields in Fig. 3.3 is presumably associated with the lack of galvanic contribution of the hydrate layer to the azimuthal fields. Fig. 3.8 shows inline and broadside responses for a model with a 50 m-thick hydrate layer. The hydrate signal decreases because the volume of the hydrate layer is half of the original model (100 m-thick hydrate layer) resulting in the reduction of inductive effects significantly.

In many recent survey cruises, the transmitter is towed less than 50 m above the seafloor (e.g., Johansen et al., 2005; MacGregor et al., 2006). As I would expect, the towing altitude of the HED source has a significant effect on

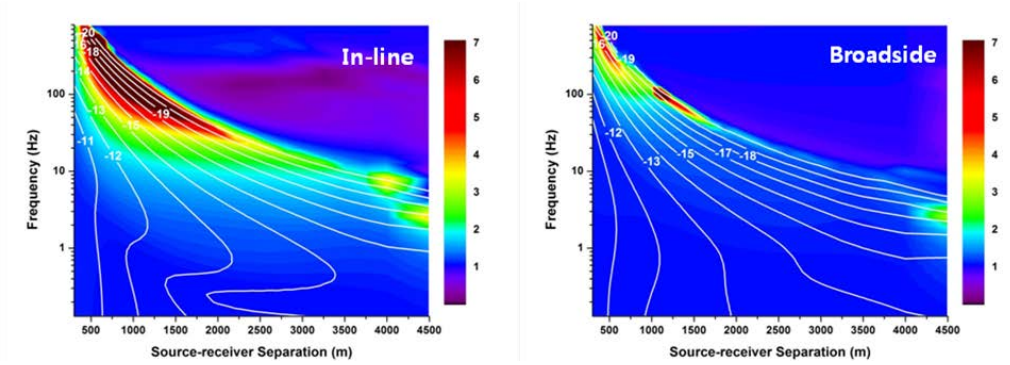

Fig. 3.8. Normalized amplitude (in color shade) and amplitude difference (in line contour, $VA^{-1}m^{-2}$) in azimuthal mode for a model with a 50 m-thick hydrate layer. The hydrate layer is buried at a depth of 50 m. A 100 m-long dipole source is situated at 100 m above the seafloor.

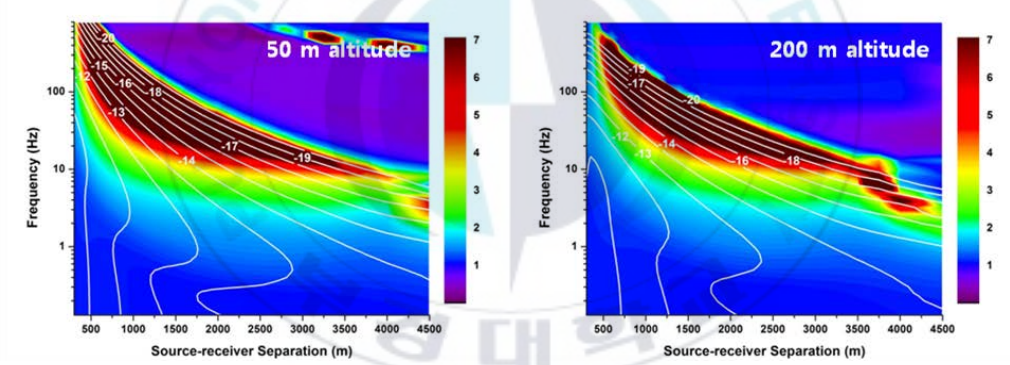

Fig. 3.9. Normalized amplitude (in color shade) and amplitude difference (in line contour, $VA^{-1}m^{-2}$) for the hydrate model in Fig. 3.2. The hydrate layer is buried at a depth of 50 m. A 100 m-long dipole source is situated at 50 m (left) and 200 m (right) above the seafloor.

the target signal. Comparing Fig. 3.9 to Fig. 3.3, we can see larger signals especially at higher frequencies as the transmitter is lowered. At low

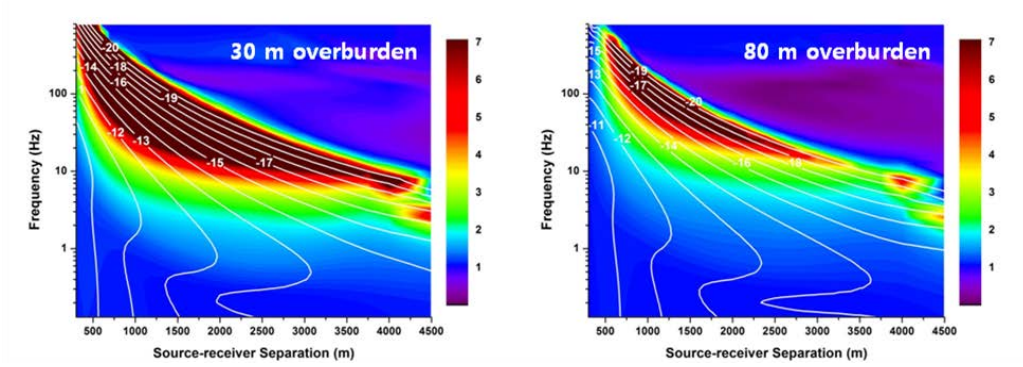

Fig. 3.10. Normalized amplitude (in color shade) and amplitude difference (in line contour, $VA^{-1}m^{-2}$) for the hydrate model in Fig. 3.2. The hydrate layer is buried at depths of 30 m (left) and 80 m (right). A 100 m-long dipole source is situated at 100 m above the seafloor.

frequencies less than 10 Hz, however, the region of amplitude differences more than 10^{-15} $VA^{-1}m^{-2}$ is almost invariant to the source altitude.

Since the base of HSZ is generally identified in a seismic section by the occurrence of BSR, it is important to determine the diffuse upper boundary for evaluating the total mass of hydrate. As expected, the target signal is enhanced as the burial depth becomes shallow and vice versa (Fig. 3.10). Note that if BSR is formed at a deeper place than the hydrate model in Fig. 3.2, and so the thickness of the hydrate layer is increased, the hydrate signal would be also enhanced as shown in Weitemeyer et al. (2006, Fig. 3.3).

3.4. Discussion and conclusions

Marine CSEM methods have become an important and valuable tool in the detection of offshore hydrocarbon targets. Oil, gas and gas hydrate increase the formation resistivity of a sediment layer if they form in sufficient quantity to block previously interconnected pore space. Simple 1D modeling is an efficient

way to establish the optimum frequency and obtain an indication of the likely source-receiver offsets necessary to detect target (Constable and Weiss, 2006). In this study, a computer program has been developed to evaluate EM responses for a 1D model with multiple source and receiver dipoles that are finite in length. Using this code, I conducted numerical analysis to design optimum field system parameters for detecting a gas hydrate layer in the shallow section.

In this Chapter, I used normalized amplitude and amplitude difference of EM fields simultaneously in determining the detection capability of the hydrate layer. The normalized amplitude can be numerically large, but care should be taken to make sure whether or not the field can actually be measured. A large normalized amplitude is detectable at high frequencies more than 10 Hz and short offsets less than 2000 m. These frequencies and offsets will be best to distinguish the top of hydrate. At the same time, we can find that there are plenty of useful offset ranges and frequencies where amplitude difference is large enough to detect the hydrate layer. Furthermore, an effect of airwaves is almost absent in amplitude difference.

Because the useful hydrate signal can be obtained at short offsets, it may be dangerous to ignore the effect of dipole length. When a point source is used for a background model, to which real field data are normalized, the target signal is distorted especially at higher frequencies and longer dipoles as shown in Fig. 3.4. As a result, the thickness of the hydrate layer would be overestimated because elevated electric-field responses especially at short offsets persist indefinitely off the upper boundary of the target layer. In addition, navigation plays a key component in gas-hydrate detection because navigation errors are more significant at short offsets than at long ranges (Weitemeyer et al., 2006). In contrast, the adverse effect of airwaves in marine CSEM data, as has been widely recognized in the oil exploration, can be avoided by acquiring data at shorter offsets.

In the case of a deep thin resistive body, the radial mode has a larger

response than the azimuthal mode (Eidesmo et al., 2002; Constable and Weiss, 2006). This occurs at relatively low frequencies in which CSEM fields are dominated by the galvanic response of the oil reservoir generated by the vertical currents of the radial mode. In the case of a shallow resistive body, however, the frequency used is high enough that inductive effects in the hydrate layer produce a significant response in the azimuthal mode as shown in Fig. 3.6. In the radial mode, we can expect galvanic effects at relatively low frequencies so that the radial fields are larger than the azimuthal fields.

In practice, one may expect such a hydrate layer to be restricted in all its dimensions and heterogeneous. This may necessitate evaluation of the response of realistic 3D structures containing gas hydrate. It is well known that smaller or larger 3D effects are present in all EM methods, especially those relying on acquisition of the electric field (Commer and Newman, 2004). Such a 3D technique will be central in future developments.

Chapter 4. Step-off, vertical electromagnetic responses of a deep resistivity layer buried in marine sediments

4.1. Introduction

The marine controlled-source electromagnetic (CSEM) method has been applied successfully to detect hydrocarbon (HC) reservoirs and to characterize gas hydrates (Ellingsrud et al., 2002; MacGregor et al., 2006, Schwalenberg et al., 2005; Weitemeyer et al., 2006). A typical marine CSEM technique uses horizontal sources and receivers with in-line geometry. At greater ranges, EM energy that has leaked into the air and propagates back to the seafloor begins to dominate the CSEM signal. This airwave effect is a consequence of the absence of attenuation in the air and more significant in shallow water (e.g., Constable 2010). Experience from land EM suggests that the best approach to dealing with the airwave is by using time-domain, instead of frequency-domain methods (Weiss, 2007; Li and Constable, 2010). Connell and Key (2012) conducted a numerical comparison of frequency domain and time-domain methods in shallow water by using a realistic frequency dependent noise model.

Two different marine CSEM methods are available in time domain (Hunziker et al., 2011). The first method uses a horizontal source for a fast data acquisition (Chave et al., 1991; Ziolkowski, 2007). A processing scheme proposed by Ziolkowski (2007), for example, deconvolves the recorded signal with the source signal, a pseudo-random binary sequence, to recover the earth impulse response. In contrast, the second method uses a vertical source for minimizing an airwave effect (Edwards et al., 1985; Holten et al., 2009). Holten et al. (2009) used a source signal consisting of eight square pulses

followed by silent periods, and the signal was stacked over these pulses to reduce noise. The recorded data at a vertical receiver due to a vertical source may have good resolution to resistive layers even at short offsets (Scholl and Edwards, 2007; Holten et al., 2009).

The difficulty when measuring vertical rather than horizontal electric fields is the small amplitude of the signal. The horizontal response from a horizontal source is 2 – 3 orders of magnitude stronger at late times than the vertical response from a vertical source (Chave and Cox, 1982). This means that both source and receiver tilt angles must be kept very small (Hunziker et al., 2011), but it is difficult to achieve the verticality of sources and receivers. However, vertical sources have the advantage of not producing an airwave, because they generate a pure transverse magnetic mode field (Um and Alumbaugh, 2007; Holten et al., 2009; Hunziker et al., 2011).

In this Chapter, I investigate vertical transient EM responses from a vertical transmitter for offshore HC reservoir models using the time-domain forward modeling code introduced in Chapter 2.

4.2. Hydrocarbon reservoir responses

I consider a 1D offshore HC reservoir model shown in Fig. 4.1, which consists of 0.3 ohm-m seawater with variable depth H_w, 1 ohm-m seafloor sediments, and a 100 m thick, 100 ohm-m HC layer at a depth of H_s below the seafloor. A 10 m-long, vertical receiver and a vertical transmitter with length L are located on the seafloor and the horizontal offset is D. In this study, the ramp time is set to be negligibly small.

The curves shown in Fig. 4.2 represent step-off responses of vertical electric fields for the HC reservoir model shown in Fig. 4.1 and a background two-layered model without the HC layer. The water thickness, reservoir depth and transmitter length are H_w = 1000 m, H_s = 1000 m and L = 100 m, respectively. The transmitter-receiver offset is D = 500 m. The electric field

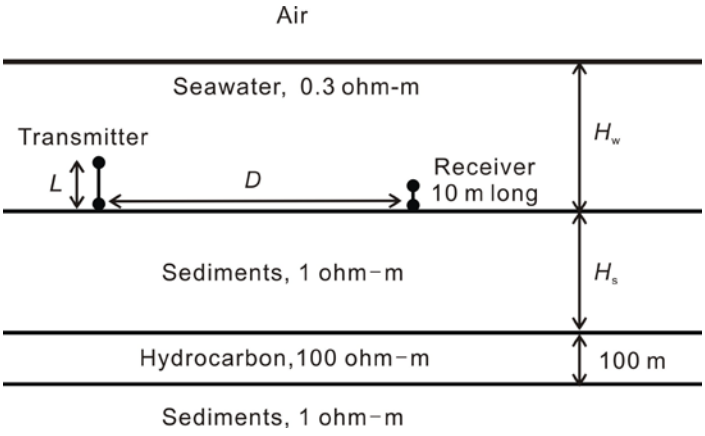

Fig. 4.1. A 1D offshore HC reservoir model.

($VA^{-2}m^{-1}$) is normalized with the source-dipole moment to make the strength of the electric field independent of the dipole length. In the illustration, absolute values of the vertical electric field are plotted, and one can see that a sign reversal of the electric field occurs at about 0.05 s.

Step-off responses are mainly galvanic at early times due to the initial current distribution, while an inductive effect dominates at late times due to the decay of induced currents. At late times t, the vertical electric field decays as $e_z(t) \sim t^{-5/2}$ in a homogeneous half-space (Ward and Hohmann, 1987). If a more resistive layer exists such as in Fig. 4.1, however, the vertical current density decays faster in time (compare the red line with the blue line in Fig. 4.2). One can see a clear anomaly compared to the response for the background model without the HC layer. In practice, the difference between the two curves is recognizable at 1 − 200 s, and the maximum contrast of more than an order of magnitude occurs at 6 s (see the gray line in Fig. 4.2) at which the electric field is well above the current instrument system noise floor, 10^{-15} $VA^{-1}m^{-2}$ (Constable and Srnka, 2007; Myer et al., 2010).

For comparison, in-line horizontal responses from a horizontal transmitter located at 50 m above the seafloor are superimposed in Fig. 4.2. The horizontal

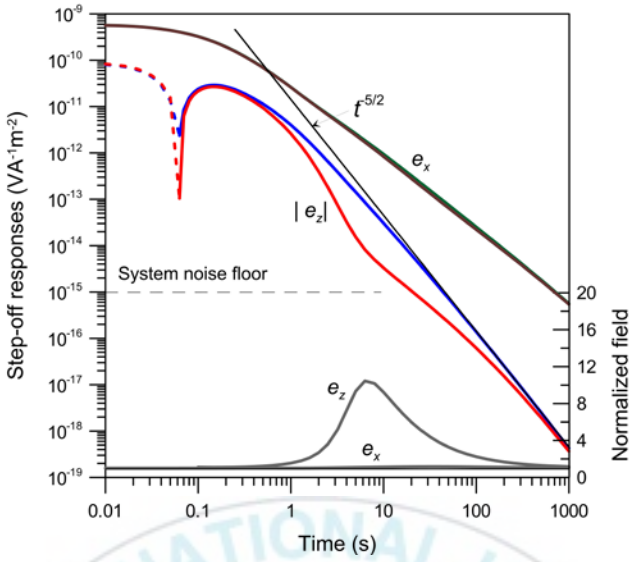

Fig. 4.2. Vertical responses from a vertical source for the HC reservoir model (red line), and the background model (blue line), and the horizontal responses from a horizontal source for the HC reservoir model (brown line) and the background model (green line). Dashed and solid lines indicate negative and positive values of the response, respectively. The bottom lines indicate the electric-field amplitudes for the HC reservoir model normalized by the responses of the background model. A 10 m-long receiver is located 500 m away from a 100 m-long transmitter at the seafloor with a water depth of 1000 m. The resistive HC layer is buried at 1000 m below the seafloor.

electric field is one (early times) ~ two or three (late times) orders of magnitude larger than the vertical electric field. In the case of the horizontal electric field, a sign reversal does not occur unlike the vertical one, and the sensitivity to the HC-layer is quite small at such a short offset. The sensitivity in the horizontal system will increase at longer offsets as indicated in Li and Constable (2010).

Fig. 4.3 represents step-off, horizontal magnetic-field responses at the

seafloor for the HC reservoir and background models. The magnetic field also shows no sign reversal as it does in the horizontal electric field. Except at early times, however, the magnetic-field curve is quite similar in shape to the vertical electric-field curve. The magnetic field also converges to a $t^{-5/2}$ response at later times. The difference between the two magnetic-field curves is recognizable at 1 − 200 s, and the maximum contrast of more than an order of magnitude occurs at 6 s at which the magnetic field is well above the system noise floor, 10^{-18} $TA^{-1}m^{-1}$ (Myer et al., 2010; Connell and Key, 2012). Magnetic-field measurements are made also in marine CSEM methods, but motion of the sensors as water currents move the receiver instrument limits the noise floor (Constable and Srnka, 2007).

Fig. 4.4 shows step-off responses for four source-receiver distances: D = 250, 500, 1000 and 2000 m. In the models, H_w, H_s and L are set to 1000 m, 1000 m and 100 m, respectively. The solid lines indicate the responses over the reservoir model with the HC layer, while the dashed lines are related to the background model without the HC layer (the water-filled reservoir model). At early times, the magnitude of electric fields decreases as an increase of the offset distance. At late times, however, all curves converge to corresponding step-off responses for either the HC- or water-filled reservoir model. The maximum contrast between the responses for the two models decreases only slightly with increasing offset distance, whereas the time of sign reversal in the electric field delays significantly, suggesting that the optimal offset is less than 2000 m for the HC reservoir model.

In Fig. 4.5, I compare step-off responses for three depths of water: H_w = 500, 1000 and 2000 m. In the models, H_s, L and D are 1000 m, 100 m and 500 m, respectively. As the sea water becomes shallow, the magnitude of electric fields decreases more rapidly at late times. The maximum contrast between the two model responses appears at 4, 6 and 16 s when H_w = 500, 1000 and 2000 m, respectively, and decreases as the depth of water increases. This result shows that the vertical-vertical CSEM method can be applied in shallow water

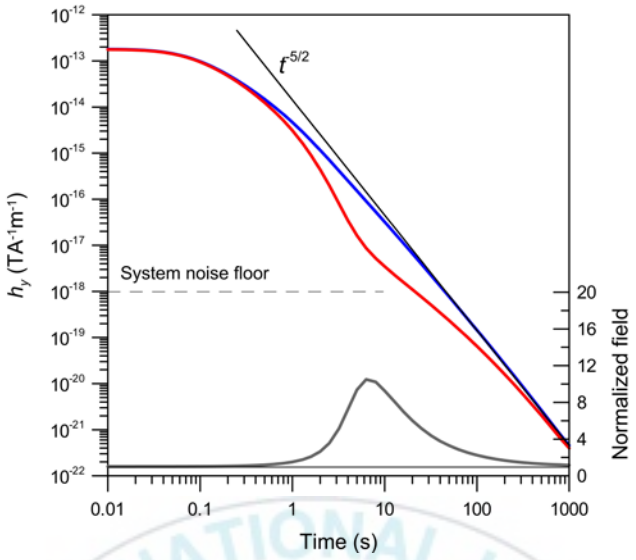

Fig. 4.3. Step-off magnetic-field responses for the HC reservoir model (red line) and the background model (blue line). The bottom gray line indicates the magnetic-field amplitude for the HC reservoir model normalized by the response of the background model. A horizontal magnetometer is located 500 m away from a 100 m-long transmitter at the seafloor with a water depth of 1000 m. The resistive HC layer is buried at 1000 m below the seafloor.

areas, although the signal approaches faster in time to the system noise floor with decreasing depth of water. In addition, noise associated with magnetotelluric signals is greater in shallow water so that the signal-to- noise (S/N) ratio would not be very high.

Next, I examine the effect of burial depths of the resistive HC layer as shown in Fig. 4.6. Three depths of the HC layer are considered: H_s = 500, 1000 and 2000 m. As the burial depth of the resistive layer becomes shallow, the magnitude of electric fields decreases more rapidly and the maximum contrast increases and appears at a faster time (4, 6, and 16 s for H_s = 500, 1000, and

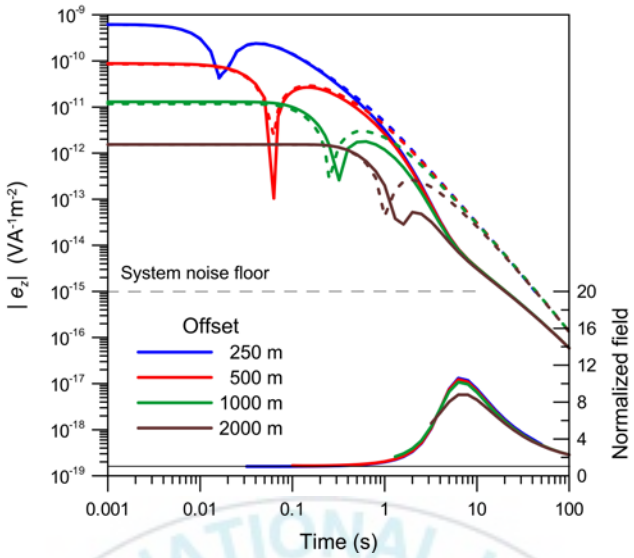

Fig. 4.4. Step-off responses for various offsets between the source and receiver over the HC reservoir model (solid lines) and the background model (dashed lines). The bottom lines indicate the ratios between the responses of the HC reservoir and the background models. A 100 m-long transmitter and 10 m-long receiver are located on the seafloor with a water depth of 1000 m. The resistive HC layer is buried at 1000 m below the seafloor.

2000 m, respectively). In the case of H_s = 2000 m, the maximum contrast occurs in close proximity of the system noise floor of about 20 s. The three step-off responses eventually fall together at late times (> 20 s).

Finally, Fig. 4.7 shows step-off responses for three lengths of the source dipole: L = 100, 200 and 400 m. Because the step-off response is normalized with the source-dipole moment, it should be independent of L if the transmitter is not too long compared with the transmitter-receiver offset. When L = 400 m, however, one can see that the effect of the source length cannot be ignored especially at early times. The magnitude is about half of that in L = 100 m at

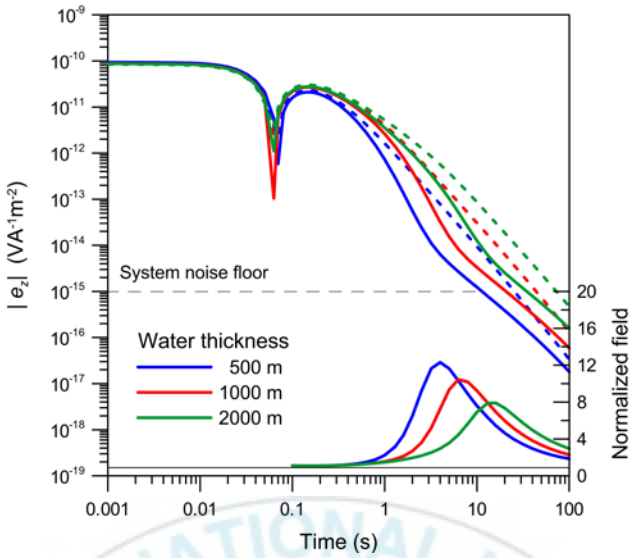

Fig. 4.5. Step-off responses for various water depths over the HC reservoir model (solid lines) and the background model (dashed lines). The bottom lines indicate the ratios between the responses of the HC reservoir and the background models. A 100 m-long transmitter and 10 m-long receiver are located on the seafloor and the offset is 500 m. The resistive HC layer is buried at 1000 m below the seafloor.

0.01 s. Through several numerical experiments, I empirically found that a point-source response is almost identical to an elongated-source response when $L/D < 0.5$, and the difference is as small as 10 %.

4.3. Discussion and conclusions

In this Chapter, I discussed the properties of a time-domain marine CSEM method with vertical transmitters and receivers through 1D forward modeling. A form of depth sounding can be made utilizing time-domain marine CSEM. In the approach with vertical transmitters and receivers, only short offsets of

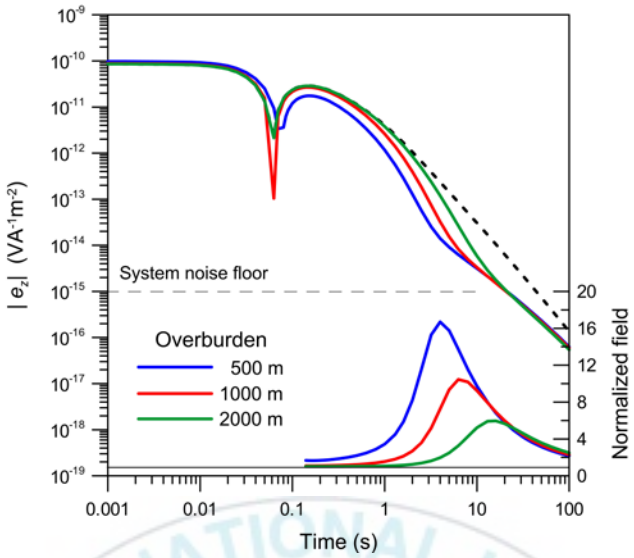

Fig. 4.6. Step-off responses for various depths of the resistive HC layer over the HC reservoir model (solid lines) and the background model (dashed line). The bottom lines indicate the ratios between the responses of the HC reservoir and the background models. A 10 m-long receiver is located 500 m away from a 100 m-long transmitter on the seafloor with a water depth of 1000 m.

transmitter and receiver are necessary as shown in Fig. 4.4 and the array therefore crosses a minimum of geological boundaries such as faults and lithological contacts. In contrast, the technique with horizontal transmitters and receivers are much more affected by near-seafloor conductivity inhomogeneities since long arrays are required. Furthermore, vertical receivers are more sensitive to the edges of a sub-seafloor resistor in comparison to CSEM with horizontal receivers (Constable and Weiss, 2006), suggesting that measurements of the vertical electric field are more suitable for mapping the lateral extent of a resistor than for recordings of the horizontal electric field.

While the vertical electric field has much smaller amplitude of signal than

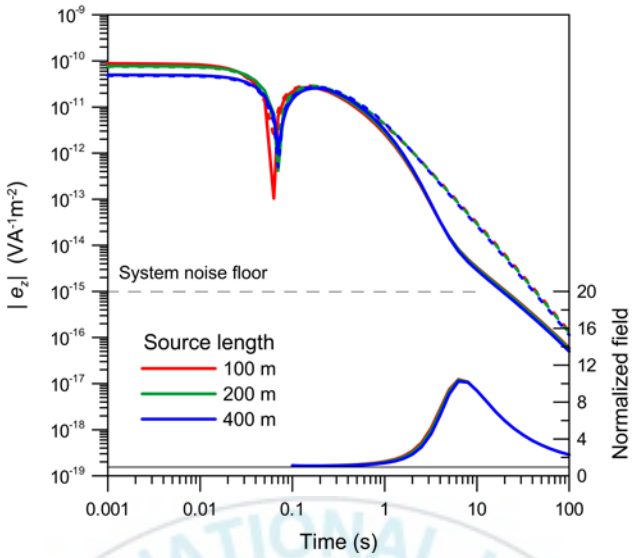

Fig. 4.7. Step-off responses for various source lengths over the HC reservoir model (solid lines) and the background model (dashed lines). The bottom lines indicate the ratios between the responses of the HC reservoir and the background models. A 10 m-long receiver is located 500 m away from the transmitter on the seafloor with a water depth of 1000 m. The resistive HC layer is buried at 1000 m below the seafloor.

the horizontal field, vertical currents resulting from a vertical transmitter are sensitive to horizontal resistive layers, yielding a faster temporal decay of electric fields as in Fig. 4.2. The modeling shows a significant difference between step-off responses of HC- and water-filled reservoirs, and the contrast can be recognized at late times at relatively short source-receiver offsets. A maximum contrast occurs at more than 4 s (Figs. 4.5 and 4.6) at which the electric field is well above the system noise floor, 10^{-15} $VA^{-1}m^{-2}$ (Constable and Srnka, 2007). Myer et al. (2010) derived the same value from a CSEM survey where 0.75 Hz signals were stacked for 60 s.

Time-domain signals are probably measurable on the seafloor, but the S/N

ratio would not be very high because noise associated with water motion and magnetotelluric signals increases with period (Constable, 2010). In the case of vertical fields, the magnetotelluric noise may be less significant since no vertical currents flow for horizontal structures, whereas the noise associated with water motion would be more important. Furthermore, the vertical antenna may be maximally coupled to horizontal water motion. In addition, a long recording window of about 200 s is required before the signal asymptotically approaches a steady state at the 500-m offset (Fig. 4.2). However, such a long trace is not practical, and the modeling shows that a short window, about 20 s, is sufficient to recover target signals which are above the noise threshold.

The lower S/N ratio results in considerable stacking times using a stationary transmitter (Connell and Key, 2012). The vertical transmitter is operated as a stationary one and is advantageous for the stacking of received signals. However, the parking of the transmitter on the seafloor would severely limit the amount of transmission locations for a given amount of ship survey time. On the other hand, the uncertainties of the location of transmitters do not lead to any time-dependent noise because the sub-seafloor response is recorded while the transmitter is turned off (Holten et al., 2009).

The time-domain method with vertical transmitters and receivers can be applied in shallow water areas. The contrast between responses of the HC reservoir and the background models increases as the sea water becomes shallow as partly shown in Fig. 4.5. In addition, acquisition with vertical transmitters and receivers eliminates airwave components from the received signal (Holten et al., 2009; Hunziker et al., 2011), which is one of the most significant challenges in shallow water.

In reality, the source dipole is not a point but has a physical extension. Because the useful HC signal can be obtained at shorter offsets, it may be dangerous if we ignore the effect of dipole length (Hunziker et al., 2011). To check how the modeling results change with an elongated source, a finite-length dipole was simulated by integration over the length of the dipole.

Because the step-off response is normalized with the source-dipole moment, it should be independent of the transmitter length (L) if the transmitter is not too long compared with the transmitter-receiver offset (D). In this study, I empirically found that a point-source response is almost identical to an elongated-source response when $L/D < 0.5$, and the difference is less than 10 %.

Chapter 5. Mapping deep-sea hydrothermal deposits with an in-loop transient electromagnetic method

5.1. Introduction

A marine controlled-source electromagnetic (CSEM) survey using an electric dipole in frequency domain has become popular for hydrocarbon (HC) exploration, where EM responses are directly related to the electrically resistive property of HC bearing strata in otherwise conductive marine sediments (Constable and Srnka, 2007; Constable, 2010). Possible targets of the marine CSEM survey, other than HC embedded in sediments, may be shallow sea-bottom sedimentation and hydrothermal mineral deposits under the deep sea. Seafloor massive sulfides (SMS) are base metal (Fe, Cu, Zn, Pb), sulfur-rich mineral deposits that are precipitated from hydrothermal fluid as it interacts with cooler ambient seawater at or beneath the seafloor at hydrothermal vent sites (Hoagland et al., 2010). Active SMS deposits are found in as many as a dozen different tectonic settings such as mid-ocean ridges, volcanic arcs, and back-arc spreading systems (Hoagland et al., 2010). However, about 61 out of 595 known hydrothermal deposits are inactive sulfide deposits, also called relict or fossil deposits (Beaulieu et al., 2010; Hannigton et al., 2011). These inactive deposits may be difficult survey targets to find because they have no detectable emissions (Dover, 2011).

The transient electromagnetic (TEM) method employs a time-varying magnetic field that is established by passing an electrical current through a closed wire loop. This primary field generates eddy currents in a conductive medium. These eddy currents are time variant as well, and they cause a

secondary EM field that can be sensed with magnetic or electric sensors placed on the seafloor or in the seawater. In TEM measurements, the secondary field, which contains information on hydrothermal deposits in the seafloor, can be measured in the absence of strong primary fields. The TEM method has excellent resolution of conductive targets at depth and uses the concept of the "smoke ring" (Nabighian and Macnae, 1991). Induced-current smoke rings of the EM field excited by an event in the transmitter diffuse outward through both the seawater and seafloor. After the current in the transmitter loop is turned off, eddy currents have diffused deeper into the seafloor with time, and the measured signal then contains information about the conductivities of the deeper layers.

Cheesman et al. (1987) and Liu and Lin (2006) calculated central loop responses for a double half-space model consisting of seawater overlying seafloor sediments. Müller et al. (2012) used a frequency-domain concentric loop system modified from a land sensor to map the magnetic susceptibility and electrical conductivity of marine surficial sediments. Swidinsky et al. (2012) examined TEM responses of in-loop and coincident-loop configurations lying at the surface of a layered seafloor, and showed that such systems are useful in determining the overburden depth to a conductive target as well as its thickness. A TEM system using a loop source may be useful to the development of compact, autonomous instruments, which are well suited to submersible-based surveys (Nakayama et al., 2011; Swidinsky et al., 2012; Nakayama and Saito, 2014). For the exploration of hydrothermal deposits, there was a recent trial using a bi-static EM sensor mounted on a remotely operated vehicle (ROV) (Goto et al., 2011). Nakayama and Saito (2014) introduced a TEM instrument operated by ROV which consists of a magneto-impedance sensor with a sensitivity of 1 pT and a 3 m × 3 m loop transmitter with 100 A of current.

In this Chapter, I investigate the possibility of applying an in-loop TEM system to the detection of marine hydrothermal deposits with a thin sediment

cover through a one-dimensional (1D) modeling and inversion study. I analyzed step-off responses of variable parameters for a layered model and compare the characteristics of horizontal and vertical loop systems for detecting a highly conductive layer. Then, two inversion techniques are tested to recover the highly conductive layer from TEM sounding data.

5.2. Hydrothermal deposits responses

In this Chapter, a hydrothermal deposit model is considered as shown in Fig. 5.1. The model consists of four layers including the seawater layer and a target hydrothermal deposit layer that is buried below a thin surficial sediment layer. The depth of seawater is set to be sufficiently large, e.g., more than 1 km, and the conductivity of the seawater is 3.3 S/m. The 10 S/m hydrothermal deposit layer with a thickness of 10 m is buried 1 m below the seafloor. The conductivity of the host sediment is 0.2 S/m. In this study, an in-loop configuration, where a dipole multi-turn receiver is located inside of the transmitter loop, is considered. The horizontal and vertical loop systems measure vertical and horizontal magnetic fields, h_z and h_y, respectively (Fig. 5.2). Allowing for the small working area of ROV, a relatively small square-loop source (2 m × 2 m), either horizontal or vertical, is located above the seafloor. However, all magnetic fields presented in this Chaper are independent of the loop size because they are normalized with respect to the source dipole moment $I \times R^2$, where I and R^2 are the strength of electric current and the area of the source loop, respectively.

Fig. 5.3 shows step-off responses of the horizontal and vertical loop systems for the hydrothermal deposit model shown in Fig. 5.1. For my purposes, the time-domain response is expressed in terms of the magnetic-field amplitude and normalized amplitude simultaneously in determining the detection capability of the hydrothermal deposit layer. The normalized amplitude is the field amplitude of a hydrothermal deposit model response normalized by that of the model without the hydrothermal deposit layer, the

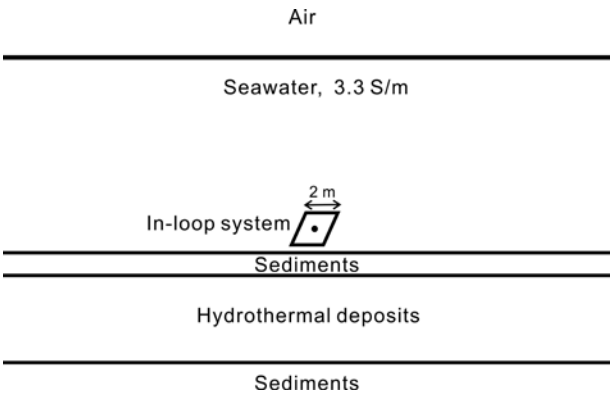

Fig. 5.1. A 4-layered deep-sea model with a hydrothermal deposit layer buried in an arbitrary depth of marine sediments. An in-loop system (with a 2-m square transmitter loop) is located above the seafloor.

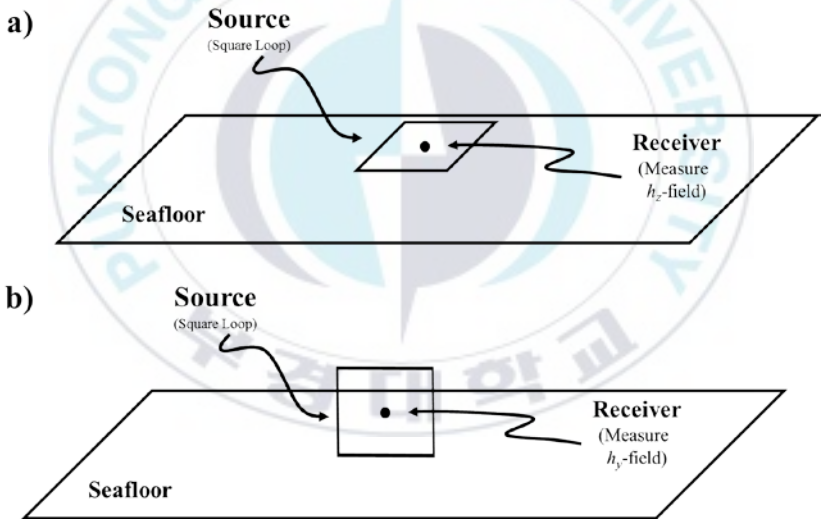

Fig. 5.2. Schematic sketch of the horizontal (a) and vertical (b) loop systems.

background model. Magnetic fields have no sign conversion in the time window considered here, 10^{-5} s – 10^{-1} s. Although the magnitude of the magnetic field is 2 – 3 times larger in the horizontal loop system than in the vertical one: $|h_z| > |h_y|$, the normalized h_z field has a slightly smaller peak value than the normalized h_y one. The target response appears earlier in h_y fields than in h_z fields; the normalized h_y field peaks at about 0.6 ms, while the corresponding h_z peaks at about 1.3 ms.

Also shown on the plot is a source normalized error floor, which is inversely proportional to the square root of time (Munkholm and Auken, 1996; Swidinsky et al., 2013), approaching 2.5×10^{-15} T/Am^2 at 1 s. This estimation is based on the magnetic sensor with a sensitivity of 1 pT introduced by Nakayama and Saito (2014) and a transmitter with a dipole moment of 400 Am^2 (2 m × 2 m loop and 100 A of current). The noise floor hits the background responses at about 13.5 ms in h_y fields and about 25.5 ms in h_z fields, respectively. This means that the target peak signals appear well above the noise level and only late-time responses would be contaminated by the system noise. The noise floor may be reduced by increasing the transmitter dipole moment.

In Fig. 5.4, I investigate step-off responses for three altitudes of the in-loop system from the seafloor: 1, 2 and 4 m. The effect of system altitudes on magnetic fields is apparent at early times especially in the background model. Target responses decay more rapidly in h_z fields than in h_y fields as the loop altitude increases. In fact, the peak value of the normalized h_y field varies only slightly until the altitude is less than about 2 m, whereas that of the normalized h_z fields decreases almost linearly as the altitude raises. Furthermore, for both fields, target responses delay over time with increasing altitude, but after peaks occur all responses converge to asymptotes. The closer the source is, the easier it is to detect the target ore layer, but the sensitivity at the 4 m altitude still maintains more than 70% of that at 1 m.

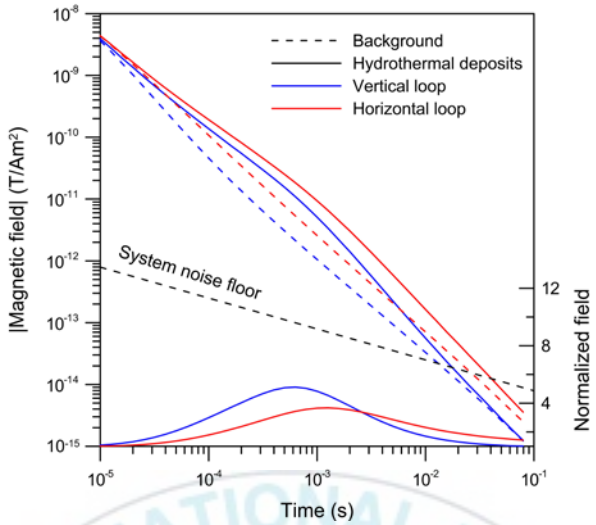

Fig. 5.3. Transient magnetic responses (upper curves) and normalized fields (lower curves) of the horizontal (red) and vertical (blue) loop systems for the deep-sea hydrothermal deposit model shown in Fig. 5.1. The solid and dashed lines indicate TEM responses for the models with and without the hydrothermal deposit layer, respectively. The 10 S/m hydrothermal deposit layer with a thickness of 10 m is buried 1 m below the seafloor. The conductivity of the host sediment is 0.2 S/m. The center of the loop system is located 2 m above the seafloor.

It may be difficult to maintain the loop system horizontally or vertically strictly with ROV. If the loop system were dipping, time-domain signals from the target layer would vary with the dip angle of the loop plane. In Fig. 5.5, magnetic fields for three dip angles of 10°, 20° and 30° are compared with the un-tilted case. The influence of dip angles is apparent in both fields perpendicular to the loop plane (which are denoted by h_y' and h_z') at early times with its maximum at about 0.3 ms for the background model (dashed lines), whereas it is greatest at about 25 ms for the hydrothermal deposit model (solid lines). As the dip angle increases, h_y' fields increase but h_z' fields decrease

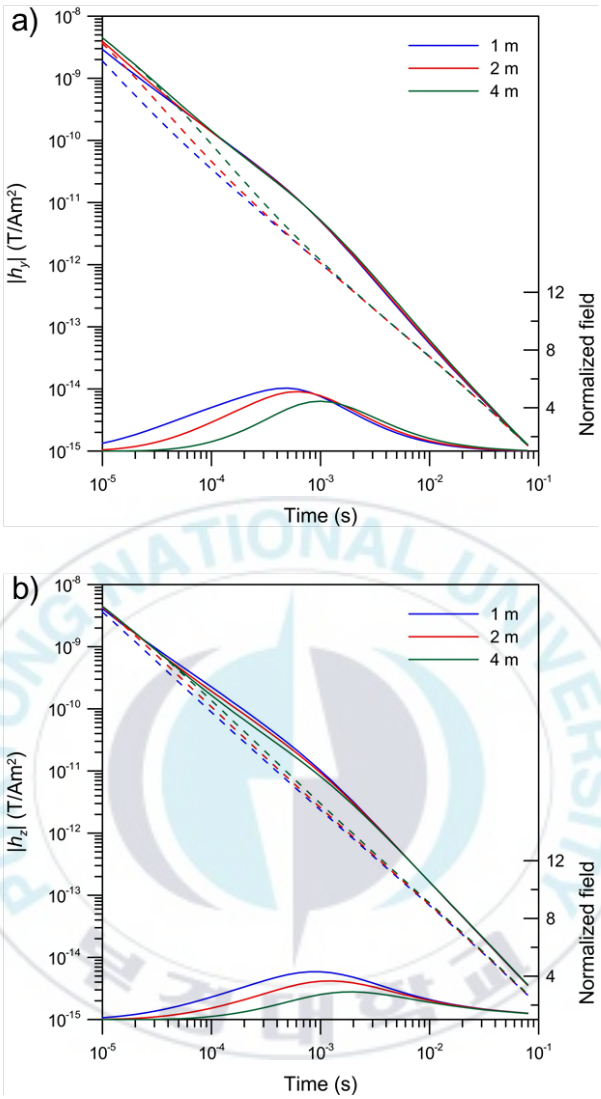

Fig. 5.4. Transient magnetic responses (upper curves) and normalized fields (lower curves) of the vertical (a) and horizontal (b) loop systems for various loop altitudes in the deep-sea hydrothermal deposit model. The 10 S/m hydrothermal deposit layer with a thickness of 10 m is buried 1 m below the seafloor. The conductivity of the host sediment is 0.2 S/m.

slightly. The h_y' field is more sensitive to the change in dip angles of the loop system than the h_z' field. Consequently, the effect of dip can probably be ignored for inclination up to about 10°, which provide only small differences from the un-tilted case less than 5 % even in h_y' fields.

Next, I examine the effect of burial depths of the hydrothermal deposit layer (Fig. 5.6). Three burial depths are considered: 0.5, 1 and 2 m. As expected, magnetic fields decrease as the hydrothermal deposit layer is buried deeper. Target responses appear earlier in h_y fields than in h_z fields, and are also larger in h_y fields than in h_z fields, but they decay faster so that both fields have nearly the same peak values at a burial depth of 2 m. The effect of the burial depth is apparent before peaks, but becomes indistinguishable quickly after peaks.

Figs. 5.7 and 5.8 show magnetic fields for variable conductivities and thicknesses of the hydrothermal deposit layer, respectively. The magnitude of the magnetic field is very sensitive to the change in conductivities, and increases rapidly with increasing conductivity due to increasing eddy currents (Fig. 5.7). Target responses are larger and appear earlier in h_y fields than in h_z fields. As the lower boundary of the hydrothermal deposit layer becomes deeper, target responses increase, but early-time responses are the same because the upper boundary is fixed to the same depth of 1 m below the seafloor (Fig. 5.8).

Finally, I calculate magnetic fields for variable conductivities of the marine sediment (Fig. 5.9). Three conductivities are considered: 0.1, 0.2 and 0.4 S/m. The magnetic fields are less sensitive to the change in conductivities of the background sediment. In particular, the vertical field has almost no sensitivity (Fig. 5.9b). This suggests that it will be difficult to recover the conductivity of the marine sediment exactly from magnetic-field data without any constraints, especially in the case of h_z data.

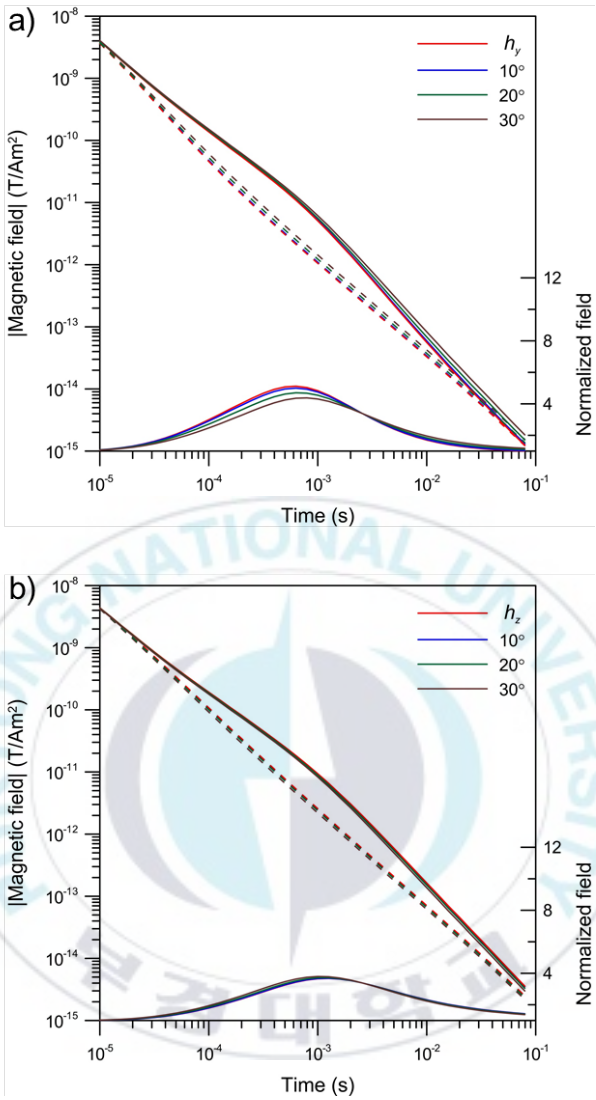

Fig. 5.5. Transient magnetic responses (upper curves) and normalized fields (lower curves) for various dip angles of the loop systems. The dip angle is measured to the vertical plane (a) and horizontal plane (b). The 10 S/m hydrothermal deposit layer with a thickness of 10 m is buried 1 m below the seafloor. The conductivity of the host sediment is 0.2 S/m.

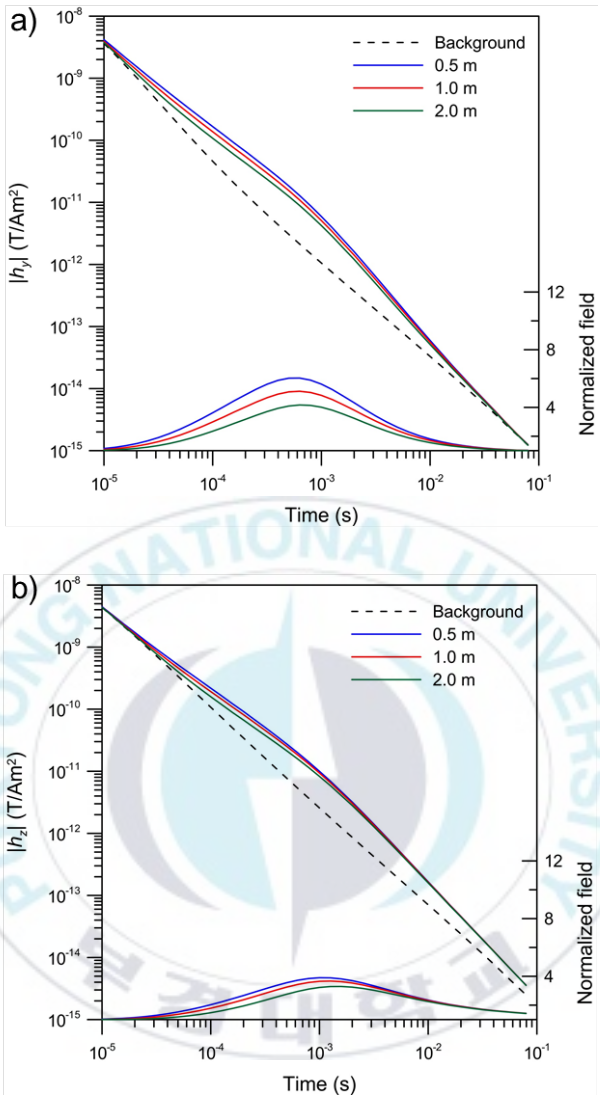

Fig. 5.6. Transient magnetic responses (upper curves) and normalized fields (lower curves) of the vertical (a) and horizontal (b) loop systems for various burial depths of the hydrothermal deposit layer. The conductivities of the host sediment and the 10-m thick hydrothermal deposit layer are 0.2 and 10 S/m, respectively. The center of the loop system is located 2 m above the seafloor.

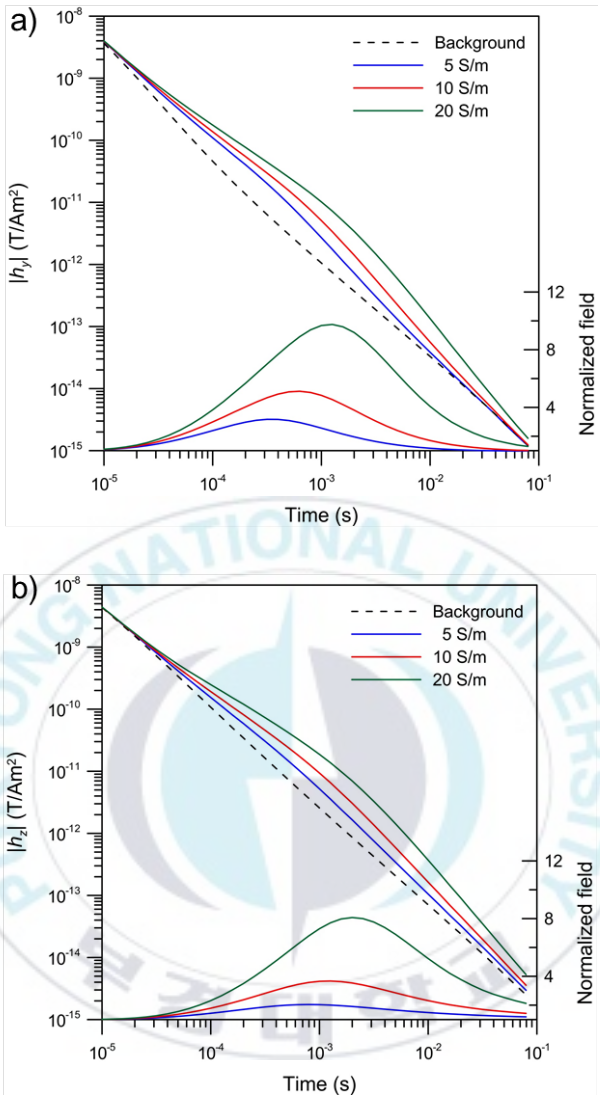

Fig. 5.7. Transient magnetic responses (upper curves) and normalized fields (lower curves) of the vertical (a) and horizontal (b) loop systems for various conductivities of the hydrothermal deposit layer. The 10 m-thick hydrothermal deposit layer is buried 1 m below the seafloor, and the conductivity of the host sediment is 0.2 S/m. The center of the loop system is located 2 m above the seafloor.

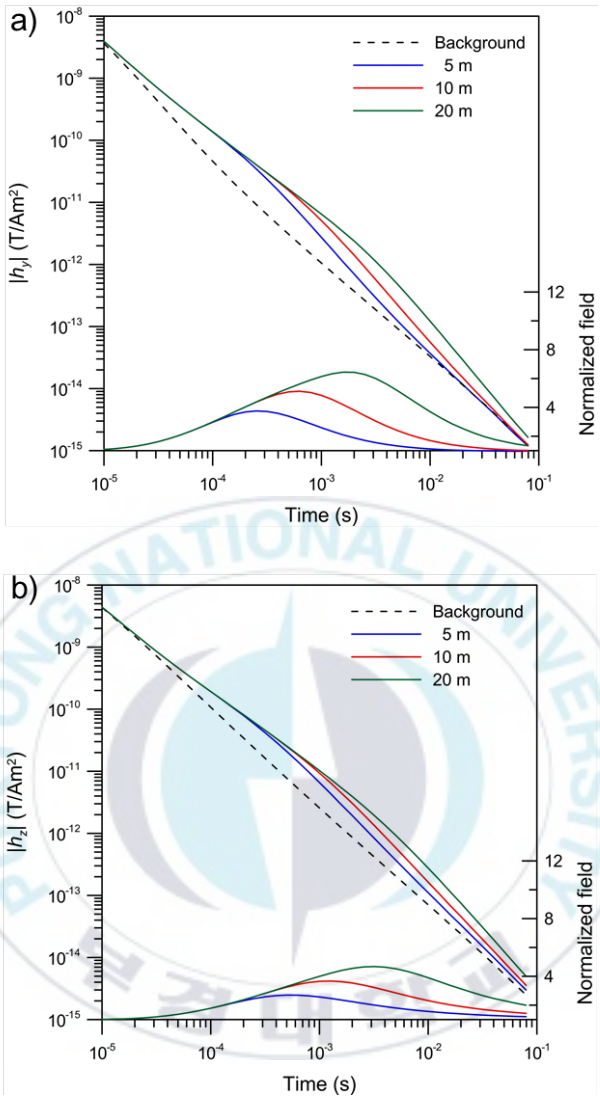

Fig. 5.8. Transient magnetic responses (upper curves) and normalized fields (lower curves) of the vertical (a) and horizontal (b) loop systems for various thicknesses of the hydrothermal deposit layer. The 10 S/m hydrothermal deposit layer is buried 1 m below the seafloor, and the conductivity of the host sediment is 0.2 S/m. The center of the loop system is located 2 m above the seafloor.

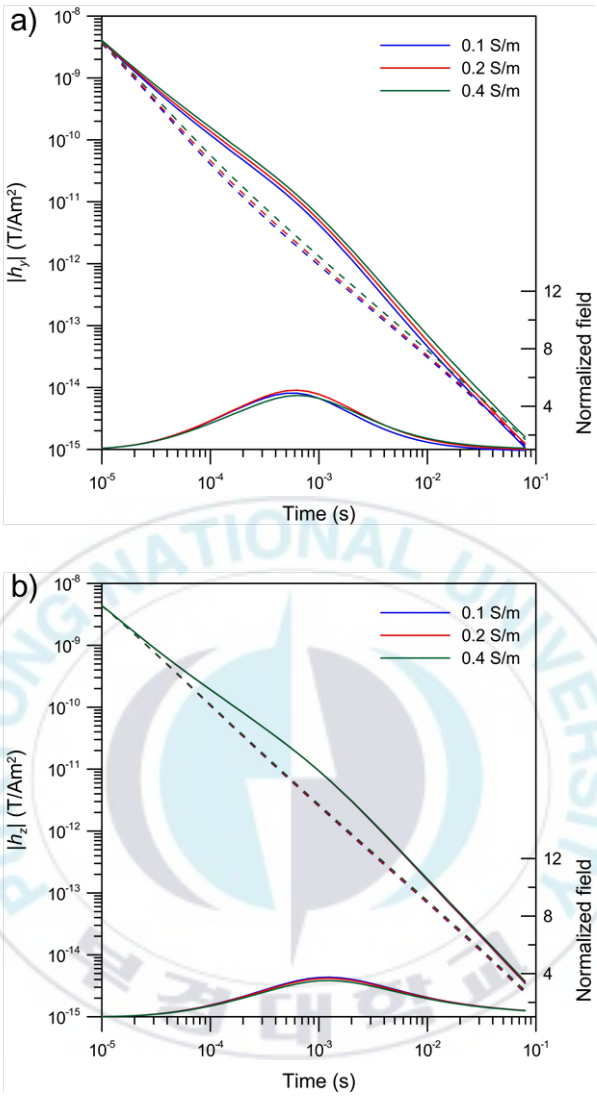

Fig. 5.9. Transient magnetic responses (upper curves) and normalized fields (lower curves) of the vertical (a) and horizontal (b) loop systems for various conductivities of the host sediment. The center of the loop system is located 2 m above the seafloor. The 10 S/m hydrothermal deposit layer with a thickness of 10 m is buried 1 m below the seafloor.

5.3. Inversion algorithm

The EM inverse problem is nonlinear with respect to subsurface electrical properties. It is generally solved iteratively, and can be linearized as

$$\Delta\mathbf{d} = \mathbf{J}\Delta\mathbf{m}, \tag{5.1}$$

where $\Delta\mathbf{d}$ is a vector of differences between observed and modeled data, $\Delta\mathbf{m}$ is a model correction vector, and $\mathbf{J}$ is a sensitivity matrix. Because equation (5.1) can be numerically unstable when solved for $\Delta\mathbf{m}$, it is necessary to impose some form of constraints on $\Delta\mathbf{m}$ to ensure the stability of the iterative process. The problem may be overcome in the damped least-squares approach by adding a constant to the principal diagonal (Marquardt, 1963). The constraint is included into an objective function to be minimized as

$$\Phi = \left\|\Delta\mathbf{d} - \mathbf{J}\Delta\mathbf{m}\right\|^2 + \lambda\left\|\Delta\mathbf{m}\right\|^2, \tag{5.2}$$

where λ is the Lagrange multiplier. Minimizing Φ in equation (5.2) produces a system of linear equations in the form of a normal equation

$$\left[\mathbf{J}^{\mathrm{T}}\mathbf{J} + \lambda\mathbf{I}\right]\Delta\mathbf{m} = \mathbf{J}^{\mathrm{T}}\Delta\mathbf{d}, \tag{5.3}$$

or in the form of an observation equation

$$\begin{bmatrix} \mathbf{J} \\ \sqrt{\lambda}\mathbf{I} \end{bmatrix}\Delta\mathbf{m} = \begin{bmatrix} \Delta\mathbf{d} \\ \mathbf{0} \end{bmatrix}, \tag{5.4}$$

where $\mathbf{I}$ is the identity matrix. Another widely used constraint is to minimize model roughness through objective function Φ (Constable et al., 1987; Han et al., 2008).

$$\Phi = \left\| \Delta \mathbf{d} - \mathbf{J}\Delta \mathbf{m} \right\|^2 + \lambda \left\| \mathbf{R}\mathbf{m}^{(k)} \right\|^2 . \tag{5.5}$$

The resulting observation equation

$$\begin{bmatrix} \mathbf{J} \\ \sqrt{\lambda}\mathbf{R} \end{bmatrix} \Delta \mathbf{m} = \begin{bmatrix} \Delta \mathbf{d} \\ -\sqrt{\lambda}\mathbf{R}\mathbf{m}^{(k)} \end{bmatrix}, \tag{5.6}$$

where **R** is a second-order difference operator quantifying model roughness and $\mathbf{m}^{(k)}$ is the model at the *k*-th iteration. The model parameter is updated to

$$\mathbf{m}^{(k+1)} = \mathbf{m}^{(k)} + \Delta \mathbf{m} . \tag{5.7}$$

The modified Gram-Schmidt method is used to solve equations (5.4) or (5.6) (Han et al., 2008). The rms data misfit can be written as

$$\psi_d = \sqrt{\frac{1}{N}\sum_{i=1}^{N} (\ln d_i - \ln d_i^m)^2} , \tag{5.8}$$

where *N* is the number of data, and *d* and d^m are the measured and modeled data, respectively. An important constraint on model parameters such as electrical conductivity or layer thickness is that they must be positive quantities. To enforce this constraint on the inverse solution, a logarithmic transformation can be used. It also has the advantage of stabilizing the solution if any parameter becomes very small (Jupp and Vozoff, 1975). The influence of the constraint is controlled by the parameter λ. In this study, selection of λ is based upon a cooling approach (Haber and Oldenburg, 1997). The process of reducing λ can then be repeated until the misfit between measured and modeled

data is reduced to an acceptable level.

5.4. Inversion tests

I tested the two inversion methods described above using synthetic data sets. The test example is the same as in Fig. 5.1, and both h_y and h_z fields shown in Fig. 5.3 are sampled at 14 logarithmically equally spaced points between 10^{-5} s and 10^{-2} s. All of the data within this time window are well above the noise floor shown in Fig. 5.3. Prior to inversion, 3% Gaussian random noise was added to the synthetic data sets. The starting model in the inversion experiment was set to a homogeneous seafloor of 2 S/m.

I first applied the damped least-squares method to the synthetic h_y and h_z data to reproduce conductivities and thicknesses of three layers below the seafloor. The convergence process is quite stable for both h_y and h_z data. The rms data misfits decrease from 0.3 for the initial guess to 0.028 after 13 iterations in the h_y data and from 0.55 for the initial guess to 0.029 after 20 iterations in the h_z data. The final misfits are slightly lower than the noise level added. Fig. 5.10 shows seafloor models inverted from the synthetic data sets. From the illustration we can see that the depth extent, conductivity and thickness of the target layer are recovered almost perfectly. However, the conductivity of the background sediment is poorly reconstructed especially h_z data, as expected from Fig. 5.9. It will be reasonable to represent the earth by a simple layered model when trying to establish the top and base of a hydrothermal deposit layer. However, it would be unfair not to say that such a good fit in this example is mainly due to the use of the model consisting of an exact number of layers.

If we have little a priori information on the number of layers, the Marquardt method may suffer from accidental discovery of unnecessarily complex solutions. Instead, Constable et al. (1987) proposed finding a smoothest model to fit the field data. Using the synthetic data sets, I examine

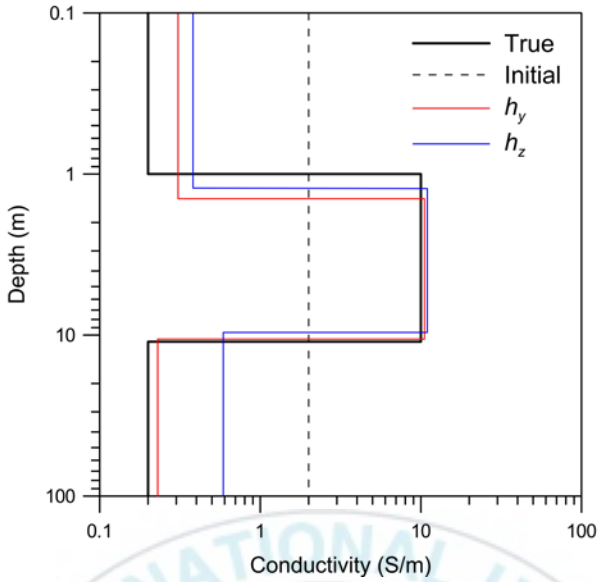

Fig. 5.10. Reconstructed models obtained from the inversion of synthetic h_y (red) and h_z (blue) data with damped least-squares method for the model shown in Fig. 5.1.

the smoothness-constrained inversion to reproduce conductivities of 10 layers that have predetermined thicknesses. The convergence process is also quite stable, and the convergence rate is also slower in the h_z data than in the h_y data. The final rms misfits are reduced to about 0.03 after 10 iterations in the h_z data and 6 iterations in the h_y data. The inverted smooth models show good agreement to the true model as shown in Fig. 5.11.

5.5. Discussion and Conclusions

I investigated the feasibility of the time-domain CSEM survey using an in-loop system for mapping marine hydrothermal deposits covered by a thin sediment layer. The magnetic-field responses generated by a loop source show a significant difference between step-off responses with and without hydrothermal deposits. If I assume the system noise floor of 2.5×10^{-15} T/Am²

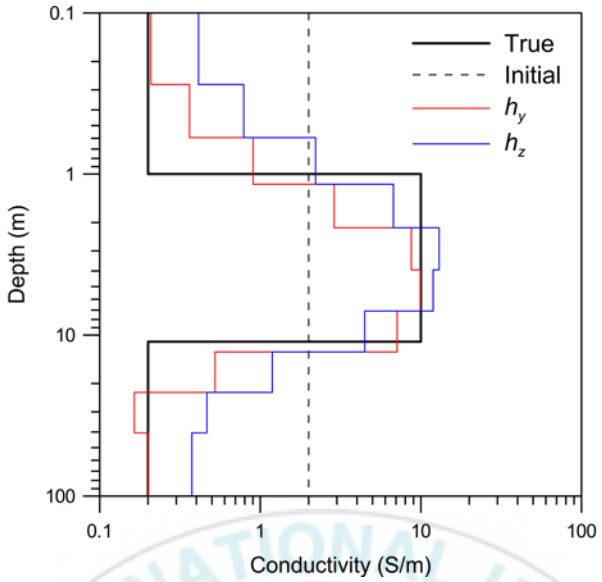

Fig. 5.11. Reconstructed models obtained from the inversion of synthetic h_y (red) and h_z (blue) data with the smoothness constraint for the model shown in Fig. 5.1.

at 1 s as shown in Fig. 5.3, the noise level hits background signals at about 13.5 ms in the h_y field and about 25.5 ms in the h_z field, which are late enough compared with the times of the peak target responses (0.6 ms and 1.3 ms). The vertical loop system is more sensitive to detect the hydrothermal deposit layer than the horizontal loop system because the target responses are larger and appear earlier in the h_y field than in the h_z field. On the other hand, the signal level is 2 – 3 times higher in the h_z field than in the h_y field. This means that the horizontal loop system is preferential to obtain a later-time magnetic field above the system noise floor than the vertical loop system. Furthermore, the horizontal loop system can be advantageous in terms of measurement stability because vertical magnetic fields are less sensitive than horizontal fields to the change in dip angles of the loop system. In addition, it may be easier to attach the horizontal loop system than the vertical one on a small ROV.

The uncertainties of the location of loop systems do not lead to any time-dependent noise associated with water motion because the marine hydrothermal deposit signal from shallow depth is recorded at relatively early times less than about 0.1 s while the transmitter is turned off. In addition, since noise associated with magnetotelluric signals decreases with water depth, the signal-to-noise (S/N) ratio of time-domain signals on the seafloor would be high (Constable, 2010). Additionally, measurements can be stacked to improve the S/N ratio.

A form of depth sounding can be made utilizing time-domain CSEM. In the deep-sea approach with ROV, only short offsets of transmitter and receiver are necessary and the array therefore crosses a minimum of geological boundaries such as faults and lithological contacts. In this study, I developed a 1D time-domain CSEM inversion program and the test example for a marine hydrothermal deposit survey demonstrated that the depth extent, conductivity and thickness of the highly conductive layer are well resolved. Analyses of the induced-polarization effect in the seafloor on time-domain measurements can be the future study of this research.

Chapter 6. Three-dimensional electromagnetic responses of disk-shaped hydrocarbon reservoir in marine sediments

6.1. Introduction

The marine controlled-source electromagnetic (CSEM) method was originally developed for deepwater studies on the oceanic lithosphere (e.g., Chave et al., 1991). With the migration of hydrocarbon (HC) exploration into the deeper water of continental slopes, marine CSEM has recently become an important exploration tool for the hydrocarbon industry (Eidesmo et al., 2002; Constable and Srnka, 2007; Constable, 2010).

These days, an interest in preliminary analysis through numerical modeling of EM responses in order to design optimal survey variables and to obtain insights about the target responses has increased with many applications of the marine CSEM method (Zhdanov, 2010; Frenkel and Davydycheva, 2012; Key, 2012; Strack, 2014). Many three-dimensional (3D) frequency-domain and time-domain EM models have been developed (Weiss and Constable, 2006; Um and Alumbaugh, 2007; Sasaki and Meju, 2009; Mittet, 2010). They are based on the finite difference method, and its main attraction is an apparent simplicity of its numerical implementation. Although the resulting linear system of equations is very large and highly sparse, the great progress in computational memory and speed makes the differential-equation technique practical for a reliable modeling tool.

Because the EM skin depth is almost always smaller in seawater than in subseafloor sediments, the EM fields measured by receivers have propagated almost entirely beneath the seafloor at a sufficiently long source-receiver offset.

However, this desirable sensitivity to subseafloor geology can be significantly lower in shallow water and at higher frequencies, where the air layer brings a stronger influence on the data. This airwave effect (energy propagating from source to receiver via the atmosphere) may be comparable or larger than the signal through the subseafloor (Um and Alumbaugh, 2007). Thus, the accurate evaluation of the airwave is essential to extract the desired information about subseafloor geology from marine CSEM measurements.

In this Chapter, I present a 3D marine CSEM modeling algorithm assuming primary EM fields as those in a homogeneous half-space to account for airwave effects exactly, and then examine the sensitivity of marine CSEM methods to a thin resistive disk-shaped target buried in the conductive media. This model represents an oil or gas reservoir in water-saturated sediments. Analysis of the disk model revealed that the in-line 3D response has a transition from the 1D four-layer response on the disk to the airwave response off the disk.

6.2. Basic algorithm

Neglecting displacement currents, a diffusion equation for the electric field is derived under quasi-static approximation as in equation (2.3). A second-order vector Helmholtz equation for the magnetic field can also be obtained from equations (2.1) and (2.2). Although the two Helmholtz equations can be solved simultaneously, this method requires a large amount of computation. Thus, in general, the electric field is obtained first from equation (2.3), and then the magnetic field is derived from equation (2.1) (e.g., Newman and Alumbaugh, 1995).

Decomposing the electric field into primary ($\mathbf{E}_p$) and secondary ($\mathbf{E}_s$) fields as

$$\mathbf{E} = \mathbf{E}_p + \mathbf{E}_s \tag{6.1}$$

yields

$$\nabla \times \nabla \times \mathbf{E}_p + i\omega\mu_0\sigma_p\mathbf{E}_p = -i\omega\mu_0\mathbf{J}_s - i\omega\nabla \times \mathbf{M}_s \quad (6.2)$$

$$\nabla \times \nabla \times \mathbf{E}_s + i\omega\mu_0\sigma\mathbf{E}_s = -i\omega\mu_0(\sigma - \sigma_p)\mathbf{E}_p \quad (6.3)$$

where σ_p indicates the conductivity of a background medium. The advantage of this approach is that we can use known analytical solutions for the background field and solve numerically the boundary-value problem for the anomalous field only (Zhdanov, 2009). Equation (6.3) also enables us to avoid a singularity problem at the source point (Unsworth et al., 1993). Weiss and Constable (2006) developed a 3D CSEM modeling algorithm using primary fields for a homogeneous whole-space. However, it may be difficult to evaluate airwave effects accurately with the algorithm using whole-space primaries.

In this study, I develop a 3D marine CSEM modeling algorithm using primary fields for a homogeneous half-space to account for airwave effects accurately (see Appendix C). I used a scheme that employs the staggered finite-difference grid to solve the second-order vector Helmholtz equation (6.3) (Yee, 1966). The resulting large, sparse linear system of equations is solved using the iterative Quasi-Minimal Residual (QMR) solver with a simple diagonal (Jacobi) pre-conditioner (e.g., Weiss and Constable, 2006). Using this code, I investigate the sensitivity of 3D EM responses to a thin disk-shaped resistive body in a conductive medium.

6.3. Disk-shaped hydrocarbon reservoir responses

In this Chapter, I use 3D forward modeling to examine the sensitivity of a marine CSEM method, and additionally I also used simple 1D modeling to show that insights obtained from the 1D calculation is appropriate when both the source and receiver are over the target of interest. Fig. 6.1 represents a 4-layered 1D model with a HC reservoir in marine sediments. In the model, a 100 m-thick HC layer of 100 ohm-m resistivity buried 1 km below the seafloor. The

resistivities of the seawater and the sediment are 0.3 ohm-m and 1 ohm-m, respectively. The positive *z* axis points downward with the origin located at the sea surface. The depth of seawater is 1 km. A horizontal electric dipole source with a transmission frequency of 1 Hz is located 100 m above the seafloor (z = 0.9 km) and receivers are on the seafloor with in-line geometry.

Fig. 6.2 shows electric-field amplitudes of the radial mode for the 4-layer model shown in Fig. 6.1. The 1D EM responses were calculated using the code developed by Lee et al. (2011). From the illustration, we can see that airwave effects are evaluated accurately from the 3D modeling algorithm using primary fields for a half space. Clearly, the agreement between 1D and 3D results for the 4-layer model does not diminish the importance of 3D modeling in data interpretation and experimental design where the lateral extent of the target is important. The agreement between the 1D and 3D calculations not only verifies the accuracy of the 3D modeling, but also shows that the 1D modeling is fairly accurate if both the source and receiver are over the circular disk and if the line connecting the source and receiver is passing over the center of the disk (Constable and Weiss, 2006). This is because the EM fields from the source decay quickly due to a combination of the $1/r^3$ (r: source-receiver distance) dipole geometry and the exponential inductive attenuation (e.g., Constable and Weiss, 2006). Therefore, the contribution from the target that is far away from the source-receiver region is very small. Note that 1D models are not appropriate when the shape of disk is not circular and its size is smaller in the cross-line direction than in the in-line direction (Tehrani and Slob, 2013).

In 3D modeling, the diameter of a disk-shaped HC reservoir and the resistivity of the host media can be found in Fig. 6.3. The EM responses from 3D modeling for a circular disk of 5-km diameter are shown in Figs. 6.5 – 6.10, 6.12 and 6.13. A disk of 10-km diameter is used as well as the one of 5-km diameter in Fig. 6.11. Infinite- and zero-diameter disks are represented by the 4- and 2-layer models, respectively. An equally spaced grid model (260 × 100 × 60) is used to calculate the electric fields for the 3D model shown in Fig. 6.3.

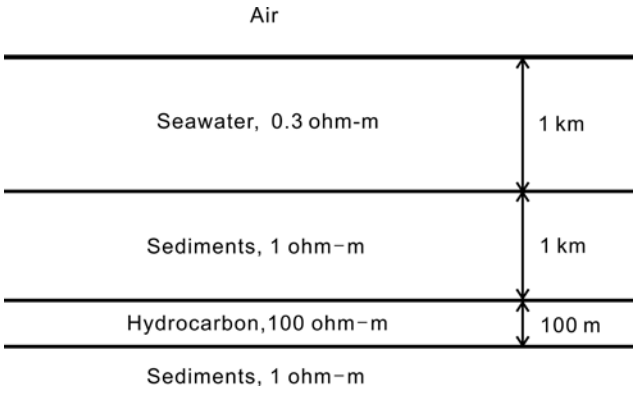

Fig. 6.1. A 4-layer offshore model with a 100-m thick hydrocarbon layer buried at a depth of 1 km in host sediments in 1 km water depth.

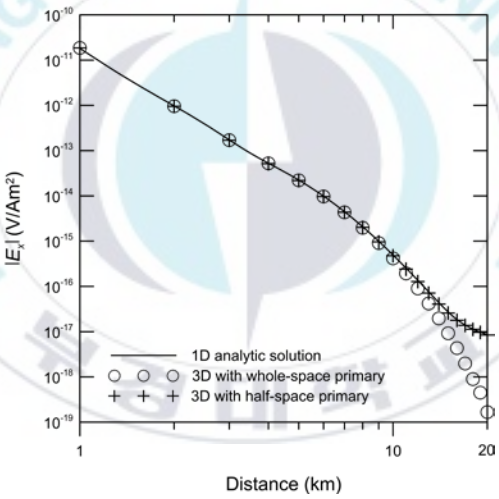

Fig. 6.2. A comparison between 3D numerical (circles and crosses) and analytic (solid line) solutions for the offshore model in Fig. 6.1 at a frequency of 1 Hz. The circle and cross symbols indicate electric fields derived from primary fields for a whole-space and half-space model, respectively. An *x*-directed electric dipole source is located 100 m above the seafloor, and receivers are located at the seafloor.

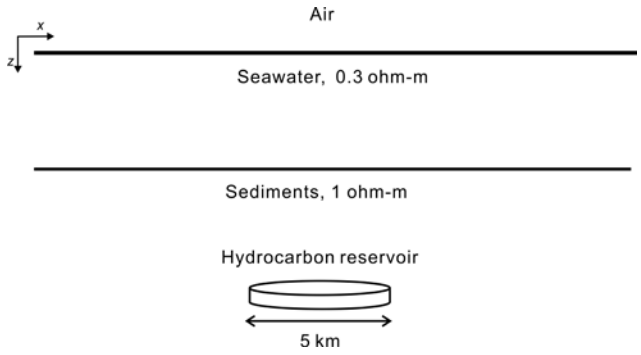

Fig. 6.3. A disk-shaped resistive reservoir with a diameter of 5 km in marine sediments.

The grid spacing is 100 m. Fig. 6.4 shows the history of QMR residuals while solving for the 3D model having a 5-km diameter disk at a frequency of 1 Hz. With the convergence criterion of the QMR residual set to 10^{-16}, 992 iterations are required and the CPU time is about 900 s to complete the calculation using a PC (Intel i7-870 CPU, 16 GB memory).

Figs. 6.5 – 6.7 show electric fields as a function of *r* at a frequency of 1 Hz for the 3D model shown in Fig. 6.3. The source is positioned over one edge of the disk in Figs. 6.5 and 6.6, and on the left side off the disk in Fig. 6.7. The electric fields are plotted along a line passing through the source and the point over the center of the disk. From these illustrations, we can see that both the amplitude and phase of the electric fields for the 3D model are almost identical to the 4-layer responses when both the source and receiver are positioned directly over the disk. The fields then fall off quickly at the same attenuation rate as for the 2-layer model without the HC layer when the receiver is positioned off the disk (Figs. 6.5 and 6.6). I define this zone, which has rapid attenuation of reservoir responses, as a transition zone. The width of the transition zone is about 3.5 km in the case of 1 km seawater.

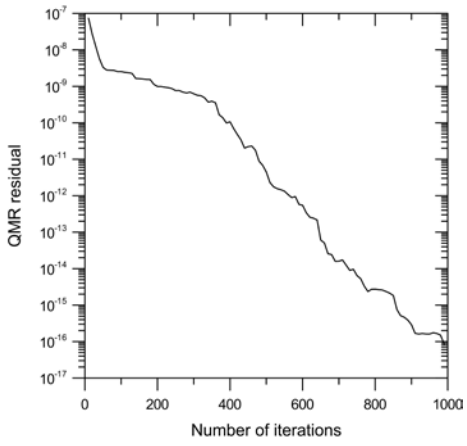

Fig. 6.4. History of QMR residuals during the problem solving for the standard 3D model having a 100 ohm-m, 5-km diameter disk-shaped reservoir shown in Fig. 6.3 at a frequency of 1 Hz.

Airwave effects eventually dominate the signal observed on the seafloor in the range of $r > 5$ km. In particular, the airwave effect can be easily found in the phase analysis rather than the amplitude analysis because the phase remains constant in the airwave range (Fig. 6.6) (Eidesmo et al., 2002). When the source is located off the disk (Fig. 6.7), the 3D responses decrease with the attenuation rate nearly parallel to the 4-layer response and converge at $r > 5$ km to that for the source located over the left edge of the disk. In the range of $r > 8$ km, the airwave effect dominates the disk signal.

In all of the examples considered below, the source is positioned over one edge of the disk. Fig. 6.8 represents the electric-field amplitudes in the disk model for various depths of seawater: 400 m, 600 m, 800 m and 1000 m. The depth of seawater is a primary factor which controls airwave effects (Eidesmo et al., 2002; Um and Alumbaugh, 2007). The transition zone shrinks from airwave effects as the depth of water becomes shallow. If the water depth is

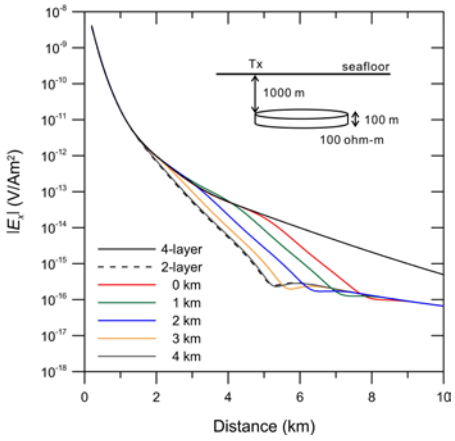

Fig. 6.5. Amplitudes of in-line electric fields at 1 Hz as a function of source-receiver distance for the disk model in Fig. 6.3 (color solid lines). The black solid and dashed lines indicate 1D 4-layer and 2-layer responses, respectively. An *x*-directed electric dipole source is located over the 100 ohm-m disk in the range of 0 - 4 km from the left edge of the disk. Both the water thickness and burial depth of the disk are 1 km.

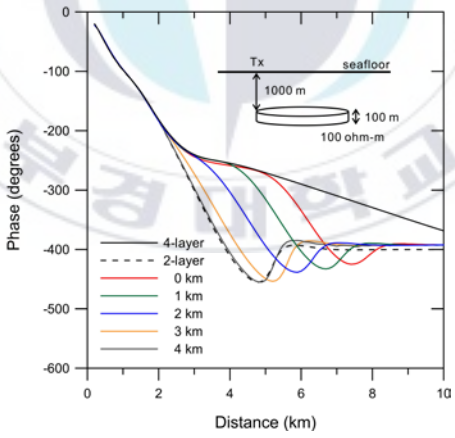

Fig. 6.6. Phases of in-line electric fields for the disk model in Fig. 6.3.

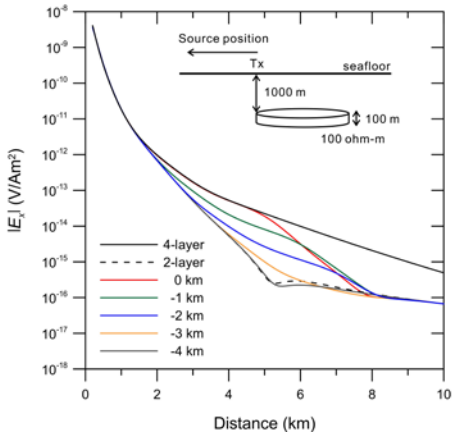

Fig. 6.7. Same as in Fig. 6.5 except that the source is located in the left side of the disk.

less than 400 m, the EM responses from the resistive disk are hardly recognized even in the case that both the source and receiver are positioned over the disk.

In Fig. 6.9, I investigate the effect of burial depths of the reservoir; the depth from the seafloor to the top of the reservoir varies from 500 m to 2 km. As expected, the sensitivity to the reservoir decreases with increasing burial depth. The target response cannot be observed when the reservoir depth becomes deeper than 2 km. Constable and Weiss (2006) suggested that a tabular target must be at least twice its burial depth in lateral extent before it is visible to the CSEM method. However, this is not valid when the burial depth is more than 2 km and the airwave effect is present.

In the next example, the source frequency varies from 0.5 Hz to 4 Hz (Fig. 6.10). As the source frequency increases, the sensitivity to the reservoir increases, whereas the amplitude eventually decreases below the current system noise floor, 10^{-15} V/Am^2 (Constable, 2010), at higher than 1 Hz. Fig. 6.11 shows the EM responses measured by the broadside array. In marine CSEM, it is well known that broadside responses are much weaker than in-line ones (e.g.,

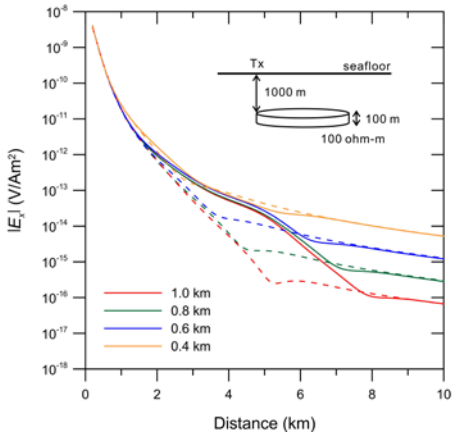

Fig. 6.8. In-line electric fields at 1 Hz for various water depths in the disk model in Fig. 6.3 (solid lines) and the 2-layer model (dashed lines). A source dipole is located over the left edge of the 100-ohm-m disk buried 1 km below the seafloor.

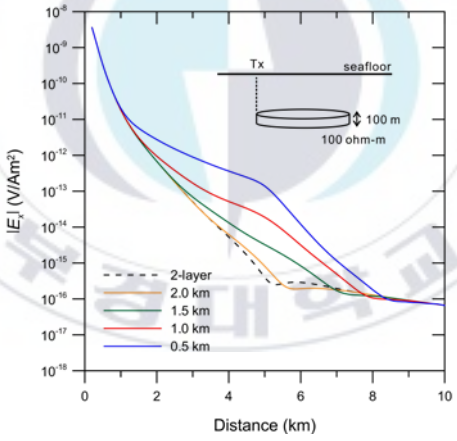

Fig. 6.9. In-line electric fields for various burial depths of the resistive disk shown in Fig. 6.3 (solid lines). The dashed line indicates 1D 2-layer responses. A source dipole is located over the left edge of the 100-ohm-m disk. The water depth is 1 km.

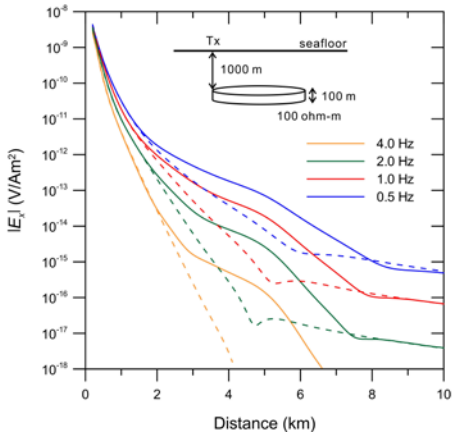

Fig. 6.10. In-line electric fields at various frequencies for the disk model in Fig. 6.3 (solid lines) and the 2-layer model (dashed lines). A source dipole is located over the left edge of the 100-ohm-m disk. The water depth is 1 km.

Eidesmo et al., 2002). In fact, the broadside electric fields even for a 10-km diameter disk model are only 5% compared to the in-line electric fields for the 5-km diameter disk model.

Finally, Figs. 6.12 and 6.13 show electric-field amplitudes for variable disk thicknesses and resistivities, respectively. The galvanic component of current flow will behave as in DC resistivity and exhibit a T-equivalence, while the inductive component of field attenuation will be sensitive to the resistivity of the target and, to some extent, be independent of thickness (Constable and Weiss, 2006). From these illustrations, we can find that the T-equivalence is almost observed at such a low frequency of 1 Hz for the thin 100 ohm-m tabular target, whose responses vary almost linearly with the target thickness and resistivity even in the transition zone. This suggests that a galvanic response accounts for almost all of the sensitivity to the thin tabular target.

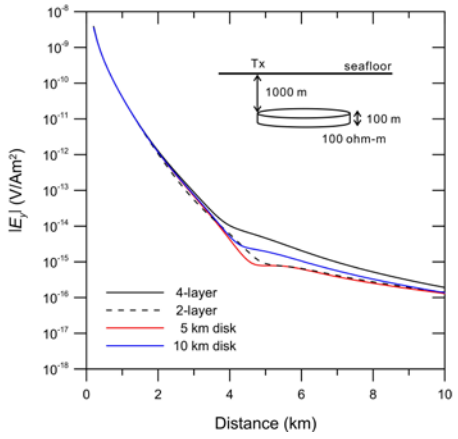

Fig. 6.11. Broadside electric fields at 1 Hz for the disk model in Fig. 6.3. The dashed line indicates 1D 2-layer responses. A source dipole is located over the left edge of the 100-ohm-m disk. The water depth is 1 km.

Use of the inductive effect is advantageous for resolving reservoir thickness and resistivity stably through an inversion process (Constable and Weiss, 2006). However, as shown in Fig. 6.10, if higher frequencies are used for more inductive effects the disk responses become lower and approach rapidly close to a noise level. The limit is 4 Hz for the model considered in this study if the instrument noise threshold is assumed to be 10^{-15} V/Am^2. The fact that the T-equivalence is fully satisfied at 0.1 Hz suggests that an available frequency range in the inversion procedure is not so wide.

6.3. Discussion and conclusions

It is well known that 3D effects exist more or less in all EM methods, especially those relying on acquisition of electric fields. In this regard, the 3D modeling is important in the interpretation of large CSEM data over targets of complicated geometry. In this Chapter, I have developed a 3D marine CSEM modeling algorithm using primary fields for a homogeneous half-space to

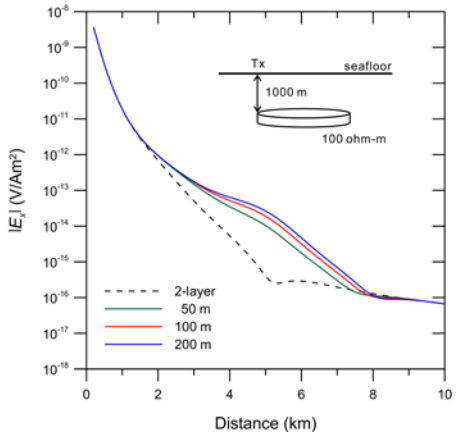

Fig. 6.12. In-line electric fields at 1 Hz for various thicknesses of the disk shown in Fig. 6.3 (solid lines). The dashed line indicates 1D 2-layer responses. A source dipole is located above the left end of the disk. Both the water thickness and the burial depth of the 100 ohm-m disk are 1 km.

accurately account for airwave effects. Sensitivity analysis for the 3D disk-shaped reservoir model in Fig. 6.3 revealed several interesting facts. Both the amplitude and phase of the electric fields at a frequency of 1 Hz for the 5-km disk model are almost identical to the 1D 4-layer model responses when both the source and receiver are over the disk. When the receiver is located off the disk, the fields fall off quickly at the same attenuation rate as for the 2-layer model without the hydrocarbon layer. Airwave effects reduce the transition zone as the water becomes shallow. The sensitivity to the reservoir increases with increasing source frequency, but the amplitude falls below the current system noise floor at higher than 1 Hz. Broadside electric fields of a 10-km diameter disk are only about 5 % of in-line electric fields of the 5-km diameter disk.

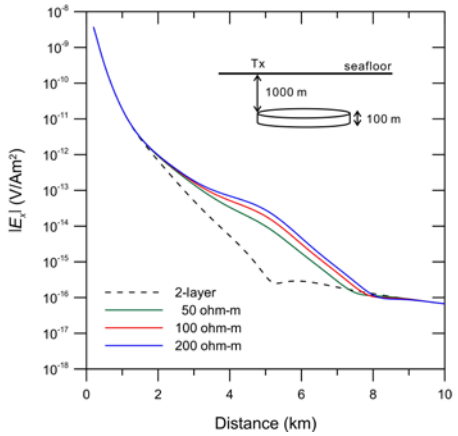

Fig. 6.13. In-line electric fields at 1 Hz for various resistivities of the disk shown in Fig. 6.3 (solid lines). The dashed line indicates 1D 2-layer responses. A source dipole is located above the left end of the disk. Both the water thickness and burial depth of the 100-m thick disk are 1 km.

Because the marine CSEM response is not completely T-equivalent, particularly at higher frequencies where inductive effects are larger, the reservoir thickness and resistivity, in principle, can be resolved separately if the measurements are well above the noise floor. However, note that CSEM data may be inverted successfully with constraints or prior structural information because they are losing resolution rapidly at depth.

Chapter 7. Conclusions

Simple 1D modeling is an efficient way to obtain an indication of the likely source–receiver offsets necessary to detect a resistive target. The time-domain EM responses can be efficiently computed by a spline interpolation and a fast Fourier transform of the frequency-domain EM responses with multiple source and receiver dipoles that are finite in length.

Using the frequency-domain code, I conducted numerical analysis to design optimum field system parameters for detecting a gas hydrate layer in the shallow section. Because the useful hydrate signal can be obtained at short offsets, it may be dangerous to ignore the effect of dipole length. When a point source is used for a background model, to which real field data are normalized, the target signal is distorted especially at higher frequencies and longer dipoles. In contrast, the adverse effect of airwaves in marine CSEM data, as has been widely recognized in the oil exploration, can be avoided by acquiring data at shorter offsets. In the case of a shallow resistive body, the frequency used is high enough that inductive effects in the hydrate layer produce a significant response in the azimuthal mode. In the radial mode, we can expect galvanic effects at relatively low frequencies so that the radial fields are larger than the azimuthal fields.

Using the time-domain code, I discussed the properties of a time-domain marine CSEM method with vertical transmitters and receivers through 1D forward modeling. The time-domain method with vertical transmitters and receivers can be applied in shallow water areas. The contrast between responses of the HC reservoir and the background models increases as the sea water becomes shallow. In addition, acquisition with vertical transmitters and receivers eliminates airwave components from the received signal, which is one of the most significant challenges in shallow water. To check how the modeling results change with an elongated source, a finite-length dipole was simulated by

integration over the length of the dipole. In this study, because the step-off response is normalized with the source-dipole moment, it should be independent of the transmitter length (L) if the transmitter is not too long compared with the transmitter-receiver offset (D). In this study, I empirically found that a point-source response is almost identical to an elongated-source response when $L/D < 0.5$, and the difference is less than 10 %.

I investigated the feasibility of the time-domain CSEM survey using an in-loop system for mapping marine hydrothermal deposits covered by a thin sediment layer. The magnetic-field responses generated by a loop source show a significant difference between step-off responses with and without hydrothermal deposits. The vertical loop system is more sensitive to detect the hydrothermal deposit layer than the horizontal loop system because the target responses are larger and appear earlier in the horizontal magnetic field (h_y) than in the vertical magnetic field (h_z). On the other hand, the signal level is $2 - 3$ times higher in the h_z field than in the h_y field. In this study, I developed a 1D time-domain CSEM inversion program and the test example for a marine hydrothermal deposit survey demonstrated that the depth extent, conductivity and thickness of the highly conductive layer are well resolved. Analyses of the induced-polarization effect in the seafloor on time-domain measurements can be the future study of this research.

It is well known that 3D effects exist more or less in all EM methods, especially those relying on acquisition of electric fields. In this regard, the 3D modeling is important in the interpretation of large CSEM data over targets of complicated geometry. Finally, I developed a 3D marine CSEM modeling algorithm using primary fields for a homogeneous half-space to accurately account for airwave effects. Sensitivity analysis for the 3D disk-shaped reservoir model revealed several interesting facts. Both the amplitude and phase of the electric fields at a frequency of 1 Hz for the 5-km disk model are almost identical to the 1D 4-layer model responses when both the source and receiver are over the disk. When the receiver is located off the disk, the fields

fall off quickly at the same attenuation rate as for the 2-layer model without the hydrocarbon layer. Airwave effects reduce the transition zone as the water becomes shallow. The sensitivity to the reservoir increases with increasing source frequency, but the amplitude falls below the current system noise floor at higher than 1 Hz. Broadside electric fields of a 10-km diameter disk are only about 5 % of in-line electric fields of the 5-km diameter disk.

References

Beaulieu, S. E. Baker, E. T., German, C. R., and Maffei, A., 2013, An authoritative global database for active submarine hydrothermal vent fields, *Geochem. Geophys. Geosyst.*, **14**, 4892–4905. doi: 10.1002/2013GC004998

Bhuyian, A. H., Landrø, M., and Johansen, S. E., 2012, 3D CSEM modeling and time-lapse sensitivity analysis for subsurface CO2 storage, *Geophysics*, **77**, E343–E355

Chave, A. D., Constable, S. C., and Edwards, R. N., 1991, Electrical exploration methods for the seafloor, *in* Nabighian, M. N., ed., *Electromagnetic Methods in Applied Geophysics, v. 2*, Soc. Expl. Geophys., 931–966.

Chave, A. D., and Cox, C. S., 1982, Controlled electromagnetic sources for measuring electrical conductivity beneath the oceans 1. Forward problem and model, *J. Geophys. Res.*, **87**, 5327–5338.

Chave, A. D., 2009, On the electromagnetic fields produced by marine frequency domain controlled sources, *Geophy. J. Int.*, **179**, 1429–1457. doi: 10.1111/j.1365-246X.2009.04367.x

Cheesman, S. J., Edwards, R. N., and Chave, A. D., 1987, On the theory of sea-floor conductivity mapping using transient electromagnetic systems, *Geophysics*, **52**, 204–217. doi: 10.1190/1.1442296

Commer, M., and Newman, G., 2004, A parallel finite-difference approach for 3D transient electromagnetic modeling with galvanic sources, *Geophysics*, **69**, 1192-1202.

Connell, D., and Key, K., 2012, A numerical comparison of time and frequency-domain marine electromagnetic methods for hydrocarbon exploration in shallow water, *Geophys. Prospect.*, **61**, 187–199. doi:

10.1111/j.1365-2478.2012.01037.x

Constable, S. C., Parker, R. L., and Constable, C. G., 1987, Occam's inversion: A practical algorithm for generating smooth models from electromagnetic sounding data, *Geophysics*, **52**, 289–300. doi: 10.1190/1.1442303

Constable, S., 2006, Marine electromagnetic methods-A new tool for offshore exploration, *The Leading Edge*, **25**, 438–444.

Constable, S., and Weiss, C. J., 2006, Mapping thin resistors and hydrocarbons with marine EM methods: Insights from 1D modeling, *Geophysics*, **71**, G43–G51.

Constable, S., and Srnka, L. J., 2007, An introduction to marine controlled-source electromagnetic methods for hydrocarbon exploration, *Geophysics*, **72**, WA3–WA12.

Constable, S., 2010, Ten years of marine CSEM for hydrocarbon exploration, *Geophysics*, **75**, A67–A81, doi: 10.1190/1.3483451

Cox, C. S., Constable S. C., Chave A. D., and Webb, S. C., 1986, Controlled-source electromagnetic sounding of the oceanic lithosphere, *Nature*, **320**, 52–54, doi:10.1038/320052a0

Dover, C. L. V., 2011, Mining seafloor massive sulphides and biodiversity: what is at risk? *ICES J. Mar. Sci.*, **68**, 341–348. doi:10.1093/icesjms/fsq086

Edwards. R. N., Law, L. K., Wolfgram, P. A., Nobes, D. C., Bone, M. N., Trigg, D. F., and DeLaurier, J. M., 1985, First results of the MOSES experiment: Sea sediment conductivity and thickness determination, Bute Inlet, British Columbia, by magnetometric offshore electrical sounding, *Geophysics*, **50**, 153–161.

Edwards, R. N., 1997, On the resource evaluation of marine gas hydrate

deposits using sea-floor transient electric dipole-dipole methods, *Geophysics*, **62**, 63–74.

Eidesmo, T., Ellingsrud, S. , MacGregor, L. M., Constable, S., Sinha, M.C., Johansen, S., Kong, F. N., and Westerdahl, H., 2002, Sea Bed Logging (SBL), a new method for remote and direct identification of hydrocarbon filled layers in deepwater areas, *First Break*, **20**, 144–152.

Ellingsrud, S., Eidesmo, T., Johansen, S., Sinha, M. C., MacGregor, L. M., and Constable, S., 2002, Remote sensing of HC layers by seabed logging (SBL): Results from a cruise offshore Angola, *The Leading Edge*, **21**, 972–982.

Frenkel, M. A., and Davydycheva, S., 2012, To CSEM or not to CSEM? Feasibility of 3D marine CSEM for detecting small targets, *The Leading Edge*, **31**, 435–446. doi: 10.1190/tle31040435.1

Gabitto, J. F., and Tsouris, C., 2010, Physical properties of gas hydrates: A review, *Journal of Thermodynamics*, Article ID 271291, 12 pages. doi:10.1155/2010/271291

Goto, T., Takekawa, J., Mikada, H., Sayanagi, K., Harada, M., Sawa, T., Tada, N., and Kasaya, T., 2011, Marine electromagnetic sounding on submarine massive sulphides using remotely operated vehicle (ROV) and autonomous underwater vehicle (AUV), *Proc. 10th SEGJ Int. Symp.*, 418–422. doi: 10.1190/segj102011-001.103

Haber, E., and Oldenburg, D., 1997, Joint inversion: a structural approach, *Inverse Problems*, **13**, 63–77. doi:10.1088/0266-5611/13/1/006

Han, N., Nam, M. J., Kim, H. J., Lee, T. J., Song, Y., and Suh, J. H., 2008, Efficient three-dimensional inversion of magnetotelluric data using approximate sensitivities, *Geophys. J. Int.*, **175**, 477–485. doi: 10.1111/j.1365-246X.2008.03894.x

Hannington, M., Jamieson, J., Monecke, T., Peterson, S., and Beaulieu, S., The

abundance of seafloor massive sulfide deposits, *Geology*, **39**, 1155–1158. doi:10.1130/G32468.1

Hoagland, P., Beaulieu, S. E., Tivey, M. A., Eggert, R. G., German, C. R., Glowka, L., and Lin, J., 2010, Deep-sea mining of seafloor massive sulfides, *Mar. Policy*, **34**, 728–732. doi:10.1016/j.marpol.2009.12.001

Holten, T., Flekkøy, E. G., Singer, B., Blixt, E. M., Hanssen, A., and Maløy, K. J., 2009, Vertical source, vertical receiver, electromagnetic technique for offshore hydrocarbon exploration, *First Break*, **27**,89–93.

Hunziker, J., Slob, E., and Mulder, W., 2011, Effects of the airwave in time-domain marine controlled-source electromagnetics, *Geophysics*,**76**, F251–F261, doi: 10.1190/1.3587222

Jang, H., Jang, H., Lee, K. H., and Kim, H. J., 2013, Step-off, vertical electromagnetic responses of a deep resistivity layer buried in marine sediments, *J. Geophys. Eng.*, **10**, 025011. doi:10.1088/1742-2132/10/2/025011

Johansen, S., Amundsen, H. E. F., Rosten, T., Ellingsrud, S. , Eidesmo, T., and Bhuyian, A. H., 2005, Subsurface hydrocarbons detected by electromagnetic sounding, *First Break*, **23**, 31–36.

Jupp, D. L. B., and Vozoff, K., 1975, Stable Iterative Methods for the Inversion of Geophysical Data, *Geophys. J. Roy. Astron. Soc.*, **42**, 957–976. doi: 10.1111/j.1365-246X.1975.tb06461.x

Kaikkonen, P., 1986, Numerical electromagnetic modeling including studies of characteristic dimensions: A review, *Surv. Geophys.*, **8**, 301–337.

Kang, S., Seol, S. J., and Byun, J., 2010, An investigation in operating and design parameters for gas hydrate exploration using marine CSEM, *J. Korean Soc. Geosystem Eng.*, **47**, 139–150. (in Koreanwith English abstract)

Kang, S., Seol, S. J., and Byun, J., 2012, A feasibility study of CO2 sequestration monitoring using the mCSEM method at a deep brineaquifer in a shallow sea, *Geophysics*, 77, E117–126, doi: 10.1190/geo2011-0089.1

Key, K., 2012, Marine electromagnetic studies of seafloor resources and tectonics, *Surv*. *Geophys*., **33**, 135–167. doi :10.1007/s10712-011-9139-x

Kim, H. J., Song, Y., and Lee, K. H., 1997, High-frequency electromagnetic inversion for a dispersive layered earth, *J*. *Geomag*. *Geoelectr*., **49**, 1439–1450.

Kong, F. N., 2007, Hankel transform filters for dipole antenna radiation in a conductive medium, *Geophys*. *Prospect*., **55**, 83–89. doi: 10.1111/j.1365-2478.2006.00585.x

Kong, F. N., Johnstad, S. E., Røsten, T., and Westerdahl, H., 2008, A 2.5D finite-element-modeling difference method for marine CSEM modeling in stratified anisotropic media, *Geophysics*, **73**, F9–F19.

Kvenvolden, K. A., 1993, Gas hydrates: Geological perspective and global change, *Rev*. *Geophys*., **31**, 173–187.

Kvenvolden, K. A., 1999, Potential effect of gas hydrate on human welfare, *Proc*. *of the National Academy of Science, USA*, **96**, 3420–3426.

Lee, K. H., Jang, H., Jang, H., and Kim, H. J., 2011, Sensitivity analysis of marine controlled-source electromagnetic methods to a shallow gas-hydrate layer with 1D forward modeling, *Geosci*. *J*., **15**, 297–303, doi: 10.1007/s12303-011-0030-z

Li, Y. G., and Constable, S., 2010, Transient electromagnetic in shallow water: insights from 1D modeling, *Chinese J*. *Geophys*., **53**, 737–742.

Liu, C., and Lin, L., 2006, Transient electromagnetic response modelling of

magnetic source on seafloor and the analysis of seawater effect, *Chinese J. Geophys*., **49**, 1726–1736. doi: 10.1002/cjg2.1001

MacGregor, L. M., Andreis, D., Tomlinson, J., and Barker, N., 2006, Controlled-source electromagnetic imaging on the Nuggets-1 reservoir, *The Leading Edge*, **25**, 984–992.

Marquardt, D. W., 1963, An algorithm for least squares estimation of nonlinear parameters, *SIAM J. Appl. Math*., **11**, 431–441. doi: 10.1137/0111030

Mittet, R., 2010, High-order finite-difference simulations of marine CSEM surveys using a correspondence principle for wave and diffusion fields, *Geophysics*, **75**, F33–F50. doi: 10.1190/1.3278525

Müller, H., Dobeneck, T., Hilgenfeldt, C., Felipo, B. S., Rey, D., and Rubio, B., 2012, Mapping the magnetic susceptibility and electric conductivity of marine surficial sediments by benthic EM profiling, *Geophysics*, **77**. 1–14. doi: 10.1190/geo2010-0129.1

Munkholm, M. S., and Auken, E., 1996, Electromagnetic noise contamination on transient electromagnetic soundings in culturally disturbed environments, *J. Environ. Eng. Geoph*., **1**, 119-127. doi: 10.4133/JEEG1.2.119

Myer, D., Constable, S., and Key, K., 2010, A marine EM survey of the Scaborough gas field, Northwest Shelf of Australia, *First Break*, **28**, 77–82.

Nabighian, M. N., and Macnae, J. C., 1991, Time domain electromagnetic prospecting methods, *in* Nabighian, M. N., ed., *Electromagnetic Methods in Applied Geophysics, v. 2*, Soc. Expl. Geophys., 427–520.

Nakayama, K., Shingyouji, T., Motoori, M., Yasui, M., Kobayashi, Y., Yamazaki, A., and Saito, A., 2011, Marine time-domain electromagnetic technologies for the ocean bottom mineral resources, *Proc. 10th SEGJ Int. Symp*., 433–436. doi: 10.1190/segj102011-

001.107

Nakayama, K., and Saito, A., 2014, Development of New Marine TDEM Systems for the Ocean Bottom Hydrothermal Deposits, *84th Annual International Meeting*, SEG, Expanded Abstracts, 850–854. doi:10.1190/segam2014-1213.1

Newman, G. A., and Alumbaugh, D. L., 1995, Frequency-domain modelling of airborne electromagnetic responses using staggered finite differences, *Geophys. Prospect.*, **43**, 1021–1042. doi: 10.1111/j.1365-2478.1995.tb00294.x

Press, W. H., Teukolsky, S. A., Vetterling, W. T., and Flannery, B. P., 1992, Numerical Recipes in Fortran, 2nd ed., Cambridge, 963p.

Robinson, E. A., 1967, Multichannel time series analysis with digital computer programs, Holden-Day, 298p.

Sasaki, Y., and Meju, M. A., 2009, Useful characteristics of shallow and deep marine CSEM responses inferred from 3D finite-difference modeling, *Geophysics*, **74**, F67–F76. doi: 10.1190/1.3168616

Scholl, C., and Edwards, R. N., 2007, Marine download to seafloor dipole-dipole electromagnetic methods and the resolution of resistive targets, *Geophysics*, **72**, WA39–WA49, doi: 10.1190/1. 2434775

Schwalenberg, K., Willoughby, E., Mir, Reza, and Edwards, R. N., 2005, Marine gas hydrate electromagnetic signatures in Cascadia and their correlation with seismic blank zones, *First Break*, **23**, 57–63.

Song, Y., Kim, H. J., and Lee, K. H., 2002, High frequency electromagnetic impedance for subsurface imaging, *Geophysics*, **67**, 501–510.

Spies, B. R., and Frischnecht, F. C., 1991, Electromagnetic sounding, *in* Nabighian, M. N., ed., *Electromagnetic Methods in Applied Geophysics, v. 2,* Soc. Expl. Geophys., 285–425.

Strack, K. M., 2014, Future directions of electromagnetic methods for hydrocarbon applications, *Surv. Geophys*., **35**, 157–177. doi: 10.1007/s10712-013-9237-z

Swidinsky, A., Hölz, S., and Jegen, M., 2012, On mapping seafloor mineral deposits with central loop transient electromagnetics, *Geophysics*, **77**, 171–184. doi: 10.1190/geo2011-0242.1

Tr'ehu, A., Torres, M., Bohrmann, G., and Colwell, F., 2006, Leg 204 Synthesis: Gas hydrate distribution and dynamics in the Central Cascadia accretionary complex, *Proc. of Ocean Drilling Program, Scientific Results*, **204**, 1–40.

Tehrani, A. M., and Slob, E., 2013, Applicability of 1D and 2.5D marine controlled source electromagnetic modelling, *Geophys. Prospect*., **61**, 602–613. doi: 10.1111/1365-2478.12019

Um, E. S., and Alumbaugh, D. L., 2007, On the physics of the marine controlled-source electromagnetic method, *Geophysics*, **72**, WA13–WA26.

Unsworth, M. J., Travis, B. J., and Chave, A. D., 1993, Electromagnetic induction by a finite electric dipole source over a 2-D earth, *Geophysics*, **58**, 198–214. doi: 10.1190/1.1443406

Ward, S. H., and Hohmann, G. W., 1987, Electromagnetic theory for geophysical applications, *in* Nabighian, M. N., ed., *Electromagnetic Methods in Applied Geophysics, v. 1*, Soc. Expl. Geophys., 203–252.

Weiss, C. J., and Constable, S., 2006, Mapping thin resistors and hydrocarbons with marine EM methods, Part II-Modeling and analysis in 3D, *Geophysics*, **71**, G321–G332.

Weiss, C. J., 2007, The fallacy of the "shallow-water problem" in marine CSEM exploration, *Geophysics*, **72**, A93–A97, doi: 10.1190/1.2786868

Weitemeyer, K., Constable, S., and Key, K., 2006, Marine EM techniques for gas-hydrate detection and hazard mitigation, *The Leading Edge*, **25**, 629–632.

Yee, K., 1966, Numerical solution of initial boundary value problems involving Maxwell's equations in isotropic media, *IEEE T. Antenn. Propag.*, **14**, 302–307. doi: 10.1109/TAP.1966.1138693

Yuan, J., and Edwards, R. N., 2000, The assessment of marine hydrates through electrical remote sounding: Hydrate without a BSR?, *Geophys. Res. Lett.*, **27**, 2397–2400.

Zhdanov, M. S., 2009, Geophysical electromagnetic theory and methods, Elsevier, Netherlands, 848 p.

Zhdanov, M.S., 2010, Electromagnetic geophysics: Notes from the past and the road ahead, *Geophysics*, **75**, 75A49–75A66. doi: 10.1190/1.3483901

Ziolkowski, A., 2007, Developments in the transient electromagnetic method, *First Break*, **25**, 99–106.

Appendix A. Waveform harmonics

The step-off waveform is treated as a box-car waveform with a long on and off time. Ramp time on both sides of the on time is an option. The duration of the on time is internally determined by the last of an output time sequence, which starts (t = 0) at the base of off-ramp. The harmonics of the step-off waveform is

$$F_{\text{Step-off}}(\omega)=\left\{\begin{array}{c}\dfrac{1}{T_{\text{r}}}\dfrac{i}{\omega}\exp\left[i\omega(T_{\text{r}}+T_{\text{on}})\right]\left[\dfrac{i}{\omega}\exp(i\omega T_{\text{r}})+T_{\text{r}}-\dfrac{i}{\omega}\right] \\ +\dfrac{i}{\omega}\exp\left[i\omega(T_{\text{r}}+T_{\text{on}})\right]\left[\exp(-i\omega T_{\text{on}})-1\right] \\ +\dfrac{1}{T_{\text{r}}}\dfrac{i}{\omega}\exp\left(i\omega T_{\text{r}}\right)\left[\dfrac{i}{\omega}\exp(-i\omega T_{\text{r}})-T_{\text{r}}-\dfrac{i}{\omega}\right], \omega\neq 0 \\ T_{\text{r}}+T_{\text{on}}, \omega=0\end{array}\right\}, \quad \text{(A1)}$$

where T_{on} and T_{r} are the on time and ramp time, respectively. The on time and off time are given equal internally, and the period of this waveform is $T = T_{\text{on}} + T_{\text{off}} + 2T_{\text{r}}$.

A variable on and off time square wave is followed by the same sequence with reversed polarity. Ramp time is an option. As is the step-off case, output time sequence starts at the base of off-ramp. The harmonics of the square waveform can be simply constructed by combination of the step-off harmonics and its phase shifted reversed polarity component as

$$F_{\text{Square}}(\omega)=\left\{\begin{array}{c}F_{\text{Square}}(\omega)\left[1-\exp(i\omega t/2)\right], \omega\neq 0 \\ 0, \omega=0\end{array}\right\}. \quad \text{(A2)}$$

The on and off time are variable, and the period of this waveform is $T = 2(T_{on} + T_{off} + 2T_r)$.

The source is a normalized Gaussian probability function defined as

$$f(t) = \sqrt{\frac{\alpha}{\pi}}\exp(-\alpha t^2).$$

It's integral over time is unity, similar to that of the Dirac delta function. As the variable α becomes large, it gets close to the delta function. The delta-ness of the waveform is controlled by a half-width of the pulse

$$t_{\text{half-width}} = \sqrt{\frac{\log 2}{\alpha}}.$$

The smaller the half-width time, the more it becomes an impulse. An output time sequence starts at the peak of the pulse. The harmonics of the Gaussian waveform is

$$F_{\text{Gaussian}}(\omega) = \begin{bmatrix} \exp(-\omega^2 / 4\alpha), \omega \neq 0 \\ 1, \omega = 0 \end{bmatrix}. \quad \text{(A3)}$$

The waveform consists of a sequence of half-sine with reversed polarity and variable off time in between. So, the period is given by $T = 2(T_{on} + T_{off})$. An output time sequence starts at the end of the positive half sine. The harmonics of the INPUT waveform is

$$F_{\text{INPUT}}(\omega) = F_0(\omega)\left[\exp(-i\omega T) - \exp(-i\omega T / 2)\right], \quad \text{(A4)}$$

where

$$F_{\mathrm{INPUT}}(\omega)=\begin{bmatrix}\dfrac{T_{\mathrm{on}}}{2}(x+iy),\ \omega\neq\dfrac{\pi}{T_{\mathrm{on}}}\\ \\ i\dfrac{T_{\mathrm{on}}}{2},\ \omega=\dfrac{\pi}{T_{\mathrm{on}}}\end{bmatrix},$$

$$x=\frac{1-\cos(\pi-\omega T_{\mathrm{on}})}{\pi-\omega T_{\mathrm{on}}}+\frac{1-\cos(\pi+\omega T_{\mathrm{on}})}{\pi+\omega T_{\mathrm{on}}},$$

$$y=\frac{\sin(\pi-\omega T_{\mathrm{on}})}{\pi-\omega T_{\mathrm{on}}}-\frac{\sin(\pi+\omega T_{\mathrm{on}})}{\pi+\omega T_{\mathrm{on}}}.$$

Appendix B. Subroutine DRUM

An example of a double-precision version of subroutine DRUM (Robinson, 1967) is given by

```
      Subroutine drum(lphz, phz)
      implicit real*8 (a-z, o-z)
      dimension phz(lphz)
      pi = 4.d0*datan(1.d0)
      pj = 0.d0
      do 40 i = 2, lphz
      if(dabs(phz(i)+pj-phz(i-1)-pi)) 40, 40, 10
10    if(phz(i)+pj-phz(i-1)) 20, 40, 30
20    pj = pj + pi*2.d0
      go to 40
30    pj = pj - pi*2.d0
40    phz(i) = phz(i) + pj
      return
      end
```

Appendix C. EM fields generated by an *x*-directed electric dipole source

The EM fields generated by an *x*-directed electric dipole source (J_x) for a homogeneous whole-space are given by (Ward and Hohmann, 1988)

$$\mathbf{E}^{J_x} = \frac{e^{-ikr}}{4\pi\sigma r^3}\left\{\left[\frac{(x-x')^2}{r^2}\mathbf{u}_x + \frac{(x-x')(y-y')}{r^2}\mathbf{u}_y + \frac{(x-x')(z-z')}{r^2}\mathbf{u}_z\right]\times \right. \\ \left. (3+3ikr-k^2r^2)-(1+ikr-k^2r^2)\mathbf{u}_x\right\}, \quad \text{(C1)}$$

$$\mathbf{H}^{J_x} = \frac{e^{-ikr}}{4\pi r^2}(1+ikr)\left(-\frac{z-z'}{r}\mathbf{u}_y + \frac{y-y'}{r}\mathbf{u}_z\right) \quad \text{(C2)}$$

where

$$r = \sqrt{(x-x')^2+(y-y')^2+(z-z')^2}$$

is the source-receiver distance, (*x*, *y*, *z)* and (*x'*, *y'*, *z'*) are the locations of the source and receiver, respectively, $\mathbf{u}_x$, $\mathbf{u}_y$, $\mathbf{u}_z$ are the unit vectors in Cartesian coordinate, and *k* (= $(-i\omega\mu\sigma)^{1/2}$) is the spatial wavenumber.

The EM fields for a homogeneous half-space are given by (Chave, 2009)

$$E_x^{J_x} = \frac{1}{4\pi\sigma}\left\{\frac{2(y-y')^2}{\rho^2}\int_0^\infty \lambda^2 e^{-u(z+z')} J_0(\lambda\rho)d\lambda \right.$$
$$+\frac{(x-x')^2-(y-y')^2}{\rho^2}\frac{2}{\rho}\int_0^\infty \lambda e^{-u(z+z')} J_1(\lambda\rho)d\lambda$$
$$+\frac{(y-y')^2-(z+z')^2}{r_s^5}e^{-ikr_s}(3+3ikr_s-k^2r_s^2)$$
$$\left.+\frac{e^{-ikr}}{r^3}\left[k^2r^2+\frac{(x-x')^2}{r^2}(3+3ikr-k^2r^2)-(1+ikr)\right]\right\}, \quad \text{(C3)}$$

$$E_y^{J_x} = \frac{(x-x')(y-y')}{4\pi\sigma}\left\{\frac{2}{\rho^2}\left[\frac{2}{\rho}\int_0^\infty \lambda e^{-u(z+z')} J_1(\lambda\rho)d\lambda - \int_0^\infty \lambda^2 e^{-u(z+z')} J_0(\lambda\rho)d\lambda\right]\right.,$$
$$\left.-\frac{e^{-ikr_s}}{r_s^5}(3+3ikr_s-k^2r_s^2)+\frac{e^{-ikr}}{r^5}(3+3ikr-k^2r^2)\right\} \quad \text{(C4)}$$

$$E_z^{J_x} = \frac{x-x'}{4\pi\sigma}\left[\frac{z+z'}{r_s^5}e^{-ikr_s}(3+3ikr_s-k^2r_s^2)+\frac{z-z'}{r^5}e^{-ikr}(3+3ikr-k^2r^2)\right], \quad \text{(C5)}$$

$$H_x^{J_x} = \frac{(x-x')(y-y')}{2\pi\rho^2}\left[\int_0^\infty \frac{\lambda^2}{u+\lambda}e^{-u(z+z')} J_0(\lambda\rho)d\lambda - \frac{2}{\rho}\int_0^\infty \frac{\lambda}{u+\lambda}e^{-u(z+z')} J_1(\lambda\rho)d\lambda\right], \quad \text{(C6)}$$

$$H_y^{J_x} = \frac{1}{4\pi}\left[\frac{2(y-y')^2}{\rho^2}\int_0^\infty \frac{\lambda^2}{u+\lambda}e^{-u(z+z')} J_0(\lambda\rho)d\lambda \right.$$
$$+\frac{(x-x')^2-(y-y')^2}{\rho^2}\frac{2}{\rho}\int_0^\infty \frac{\lambda}{u+\lambda}e^{-u(z+z')} J_1(\lambda\rho)d\lambda, \quad \text{(C7)}$$
$$\left.-\frac{z+z'}{r_s^3}e^{-ikr_s}(1+ikr_s)-\frac{z-z'}{r^3}e^{-ikr}(1+ikr)\right]$$

$$H_z^{J_x} = \frac{y-y'}{4\pi}\left[\frac{2}{\rho}\int_0^{\infty}\frac{\lambda^2}{u+\lambda}e^{-u(z-z')}J_1(\lambda\rho)d\lambda - \frac{e^{-ikr_s}}{r_s^3}(1+ikr_s)+\frac{e^{-ikr}}{r^3}(1+ikr)\right], \quad \text{(C8)}$$

where

$$\rho = \sqrt{(x-x')^2+(y-y')^2}$$

is the horizontal source-receiver distance. Only four kinds of Hankel transforms are required for calculating equations (C3) – (C8). In this study, Kong's (2007) linear filter with 61 coefficients is employed for computing the Hankel transform integral.

인공송신원 전자탐사법을 이용한 해저자원의 탐지

장한길로

부경대학교 대학원 에너지자원공학과

초록

전도성의 해양퇴적물 내에 탄화수소를 배태한 지층의 전기적 물성과 직접적으로 연관되는 전자기 반응을 측정하는 전기쌍극자를 이용한 주파수영역 해양전자탐사법은 석유탐사에서 일반적인 방법이 되었다. 퇴적물에 묻혀있는 탄화수소나 가스하이드레이트 이외에 해양전자탐사의 또 다른 탐사대상은 심해의 얕은 깊이에 있는 퇴적물과 열수광상이 될 것이다.

주파수영역과 시간영역에서 유한 길이의 다중 송수신 쌍극자에 의한 1차원 전자기 반응을 평가하기 위한 컴퓨터 프로그램을 개발하였다. 시간영역 반응은 주파수영역 반응에 고속푸리에변환(FFT)을 적용하여 효율적으로 구할 수 있다. 먼저 대수영역에서 등간격으로 한 decade 당 10개의 주파수영역 반응을 구한 후 FFT를 적용하기 위해 3차 스플라인 사이채움을 실시한다. 이 때 위상의 경우에는 스플라인 사이채움 이전에 위상곡선의 불연속이 일어나지 않도록 만들어 주어야 한다. 스플라인 사이채움된 자료는 송신전류파형과 곱말기를 한 후 FFT를 통해 시간영역 자료로 만들어진다.

주파수영역 프로그램을 이용하여 얕은 깊이의 가스하이드레이트층에 대한 해양전자탐사의 감도분석을 시도했다. 목표층을 탐지하기에 충분히 진폭 차이가 큰 영역에서 유용한 송수신 간격과 주파수가 많음을 알 수 있었다. 게다가 공기파의 영향은 진폭의 차이를 취하면 거의 나타나지 않는다.

시간영역 프로그램을 이용하여 1차원 탄화수소 저류층 모델에 대한 step-off 반응을 계산하였다. 수직전기장은 수평전기장에 비해 신호의 크기는 작지만 수직의 송신기에 의해 발생된 수직 전류는 전기비저항이 높은 층에 민감하다. 모델링

결과는 탄화수소와 해수로 포화된 저류층 사이에서 큰 차이를 보여주며, 이러한 차이는 상대적으로 짧은 송수신 간격의 후기 시간대에서 인지할 수 있다. 최대 차이는 4초 이후에 발생하며, 탄화수소층의 심도에 따라 발생시간은 지연된다.

열수광상 층서구조에 대한 step-off 반응들을 분석하고 수평과 수직 루프 시스템의 특성을 비교하였다. 과도 전자기 반응은 전기전도도가 높은 층에 대해 매우 민감함을 보여주었다. 시간영역 반응은 수평 자기장 보다 수직 자기장에서 세기가 2 – 3배 더 크지만 대상체의 반응은 수평 자기장에서 수직 자기장보다 더 크고 일찍 나타난다. 가우스-뉴튼법으로 역문제를 구성하고 감쇠와 평활화제약 최소자승법으로 풀었다. 해저 열수광상 시간영역 전자탐사에 관한 수치실험은 고전기전도도층의 두께와 전기전도도 그리고 그 깊이가 잘 구해지는 것을 보여주었다.

마지막으로 수심 1 km의 해저퇴적층 속 깊이 1 km에 두께 100 m, 지름 5 km의 디스크형 고비저항 저류층이 존재하는 경우 수평 전기쌍극자에 의한 전기장 반응을 분석하였다. 인공송신원 해양전자탐사 자료의 정확한 해석을 위하여 공기파의 영향을 고려할 수 있도록 균질 반무한공간에 대한 1차장을 이용하는 3차원 모델링 알고리듬을 작성하였다. 저류층의 3차원 효과는 일반적으로 1차원 구조 반응과 비교해 전이대(transition zone)로 나타남을 확인하였다. 이 전이대는 수심이 얕을수록 공기파의 영향으로 그 폭이 줄어든다. 송신주파수가 높을수록 디스크에 대한 감도는 커지나 전기장 크기가 작아져 1 Hz이상에서는 대부분의 반응이 현재의 시스템 잡음 수준인 10^{-15} V/Am^{2}이하로 나타났다. 평행선법 반응은 지름이 10 km가 되어도 지름 5 km 동일선법 반응의 약 5%수준에 불과했다. 전이대에서도 전기비저항과 두께 변화에 대한 반응이 거의 선형적으로 변화하는 T-equivalence 현상이 얇은 판상 저항체에 대하여 1 Hz와 같은 낮은 주파수에서는 관측된다.

주요어: 해양 인공송신원 전자탐사, 가스하이드레이트, 탄화수소 저류암, 공기파, 열수광상, 과도 전자기

감사의 글

가장 먼저 김희준 교수님의 지도 없이는 이러한 큰 결실을 이루지 못 했을 것입니다. 학문적 가르침뿐 만 아니라 세상을 바라보는 시각에 큰 전환점을 마련해주신 김희준 교수님께 가장 먼저 감사의 말씀을 드립니다. 그리고 지금은 미국에 계시는 이기하 박사님에게 큰 감사의 말씀을 전하고 싶습니다. 그리고 바쁘신 와중에도 저의 학위논문 심사를 맡아주고 더 좋은 논문이 될 수 있도록 세심한 지적과 조언을 아끼지 않으신 이태종 박사님, 손정술 박사님, 남명진 교수님 그리고 하완수 교수님께 감사 드립니다. 그리고 항상 본인의 제자처럼 챙겨주시는 한양대학교의 변중무 교수님, 설순지 교수님, 정용현 교수님의 큰 도움으로 이 논문을 완성할 수 있었습니다.

학부에서부터 대학원까지 많은 가르침을 주신 공영세 교수님, 김대철 교수님, 조태진 교수님, 이광훈 교수님, 엄정기 교수님, 왕수균 교수님, 김선옥 교수님, 최요순 교수님께 감사 드립니다. 대학원 기간 동안 가장 큰 도움을 주신 박미경 박사님, 이동성 박사님 그리고 김성우 박사님, 명자 누나에게도 고마운 마음을 전하고 싶습니다. 그리고 저를 박사의 길로 인도해주시고 정말 많은 도움을 주신 최지향 박사님, 한누리 박사님, 이제는 CEO가 된 우성선배, 성화선배, 도완선배, 범임선배, 승조선배 그리고 전자탐사연구실을 거쳐간 모든 선후배님들 감사합니다. 학과 조교로 근무하면서 많은 도움을 준 은정이 누나와 은두 그리고 김한길 조교에게도 신세를 많이 졌습니다. 감사합니다. 에너지자원공학과 선후배 그리고 동기들인 보연선배, 영환이, 현교, 기주, 성훈이, 소라, 화랑이, 지후, 성재, 세범이, 진영이, 현규, 현주, 동현이, 보영이, 세빈이, 보경이, 지수, 아름이, 지은이, 채영이 이하 모두의 앞날에 좋은 일들이 많이 생기길 바랍니다.

지질자원연구원에 들르면 항상 반겨주시고 많은 조언을 해주시는 이상규 박사님, 성낙훈 박사님, 김정호 박사님, 박삼규 박사님, 김창렬 박사님, 정현기 박사님, 박인화 박사님, 송윤호 박사님, 황세호 박사님, 이성곤 박사님, 조성준 박사님, 이명종 박사님, 박계순 박사님, 박종명 박사님, 방은석 박사님, 강웅 박사님들께 정말 많은 도움을 받았습니다. 잊지 않겠습니다.

항상 외로운 나를 잘 챙겨주는 동료, 선후배들인 공주대 승욱이형, 강원대 만호, 부경대 샛별이, 한양대 상민이형, 형욱이형, 정민이형, 택현이형, 규보,

지훈이, 보나, 민호, 도완, 석민이, 캐나다에 있는 서기 그리고 연구소로 자리를 옮긴 용환이형, 명선이형 그리고 수철이형 모두 감사합니다.

고등학교, 대학교를 거쳐오는 동안 변함없는 우정을 나누고 있는 공현식, 구민수, 김도현, 김성훈, 김재경, 김희식, 나호성, 박덕홍, 방성환, 서영환, 서용환, 손장욱, 오영준, 이수민, 이승규, 이승윤, 이태훈, 임지원, 정균채, 정문재, 정호열, 하성민, 한대현, 홍현표에게도 고맙다는 말을 건네고 싶네요.

마지막으로 이 논문을 쓰는 동안 뒤에서 나를 가장 많이 도와준 연구실 선배이자 나의 하나밖에 없는 누나 장한누리와 정훈이형 그리고 부모님께 이 논문을 바칩니다.